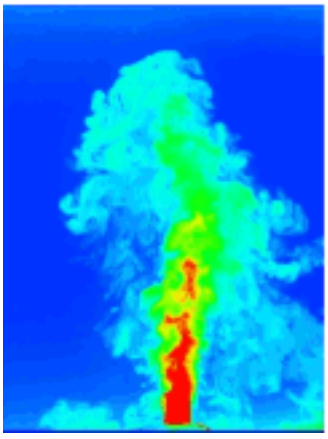

Journal of Turbulence
Publication details, including instructions for authors and subscription information:
http://www.tandfonline.com/loi/tjot20

Transverse injection of a plane-reacting jet into compressible turbulent channel flow

Christoph Schaupp [a], Rainer Friedrich [a] & Holger Foysi [b]

[a] Lehrstuhl für Aerodynamik und Strömungsmechanik, Technische Universität München, Garching, Germany

[b] Lehrstuhl für Strömungsmechanik, Universität Siegen, Siegen, Germany

Version of record first published: 06 Jul 2012

To cite this article: Christoph Schaupp, Rainer Friedrich & Holger Foysi (2012): Transverse injection of a plane-reacting jet into compressible turbulent channel flow, Journal of Turbulence, 13, N24

To link to this article: http://dx.doi.org/10.1080/14685248.2012.689430

Journal of Turbulence
Vol. 13, No. 24, 2012, 1–40

Transverse injection of a plane-reacting jet into compressible turbulent channel flow

Christoph Schaupp[a], Rainer Friedrich[a*] and Holger Foysi[b]

[a]*Lehrstuhl für Aerodynamik und Strömungsmechanik, Technische Universität München, Garching, Germany;* [b]*Lehrstuhl für Strömungsmechanik, Universität Siegen, Siegen, Germany*

(*Received 9 February 2012; final version received 19 April 2012*)

A semi-implicit large-eddy simulation technique is used to predict transport and infinitely fast reaction processes of an H_2/N_2 jet injected through a narrow spanwise slot into a subsonic turbulent air flow between isothermal channel walls. The large-eddy simulation (LES) technique is based on approximate deconvolution and explicit modelling of the filtered heat release term. Spatial derivatives are computed using sixth-order accurate central compact schemes. An explicit fourth-order Runge–Kutta algorithm serves for time-integration. Turbulent inflow conditions are generated by a separate LES of fully developed channel flow and are introduced well upstream of the injection station using characteristic boundary conditions. The complex transport processes in the vicinity of the injection region are highlighted by instantaneous and statistically averaged flow quantities by Reynolds stress and total enthalpy balances.

Keywords: compressible turbulence; large-eddy simulation; reacting turbulent flow; turbulent heat and mass transfer; turbulent mixing

1. Background

One central characteristic of the flow fields encountered in ramjet and scramjet engines is the transverse injection of a fuel jet into compressible turbulent flow. This situation is usually termed as the *jet in crossflow*. Injection of mostly gaseous fuels into the air stream may be performed from ports in the duct wall or from orifices in pylons or struts, which extend into the flow.

In the past, many studies have been reported on such transversely injected jets. A large part of this work has concentrated on perpendicular injection through circular ports in a wall, although other configurations (injection through elliptical, rectangular or slot-shaped openings, through arrangements of several ports as well as injection at angles different from 90°) have sometimes been dealt with.

The vortical structures associated with the flow field of the circular jet in crossflow have been described by Fric and Roshko [1], who distinguish four characteristic types thereof: vortices in the upstream and downstream shear layer of the injected jet; horseshoe vortices at the upstream side of the jet and close to the wall, wrapping around the jet; vortices in the jet's wake; and a counter-rotating, large-scale vortex pair (often referred to as CVP) dominating in the far field downstream of the injection location.

*Corresponding author. Email: r.friedrich@lrz.tum.de

ISSN: 1468-5248 online only

http://dx.doi.org/10.1080/14685248.2012.689430
http://www.tandfonline.com

Andreopoulos and Rodi [2] reported measurements of mean velocities, turbulent kinetic energy, turbulent shear stresses and the contributions to the balance of the turbulent kinetic energy for a round, wall-normally injected jet in crossflow, which was studied in a wind tunnel. New et al. [3] have conducted an experiment in a water channel in order to study the influence the velocity profile (of parabolic or almost top-hat shape) in the port exit section has on the flow field of the injected jet. In another experimental study of the wall-normal, round jet in crossflow by Shan and Dimotakis [4], the behavior of an injected scalar has been analyzed.

Su and Mungal [5] also experimentally studied the round jet in crossflow. They injected nitrogen into air through a pipe of circular cross section. In one configuration, the pipe's exit was arranged in the wall plane, while in another configuration, the pipe extended in the wall-normal direction from the wall through the crossflow boundary layer into the outer flow. It is to be noted that in the experiment conducted by Su and Mungal [5], the flow conditions were chosen such that the absence of a crossflow would cause the condition of fully developed turbulent pipe flow to be reached in the pipe's exit section. They made observations on the mean flow, the components of the Reynolds stresses as well as on scalar fluxes and scalar variance.

In addition, a number of numerical simulations of the jet in crossflow have been reported. Jones and Wille [6] performed an incompressible large-eddy simulation (LES) of the transverse injection of a plane jet into a channel, both streams consisting of air. They employed a finite volume formulation and used central differences of second-order accuracy for convective terms.

Large-eddy simulations for an incompressible round jet in crossflow have been reported by Yuan et al. [7], who discussed the vortical structures captured in these simulations in detail. In addition to the mean flow, turbulent kinetic energy and Reynolds stresses have been analyzed as well.

The angle of injection of the round transverse jet has been varied from wall-normal to inclined toward the upstream or downstream direction in a study by Wegner et al. [8]. Using a finite volume formulation, which was second-order accurate and included the transport of a passive scalar, they conducted LES of these configurations in order to elucidate the mixing properties of such jets.

Incompressible direct numerical simulation (DNS) of the wall-normal injection through an orifice of square cross section has been performed by Sau et al. [9], who used a finite volume method on a uniform Cartesian grid, convective terms being discretized using an upwind procedure of third-order accuracy, while for diffusive contributions, a fourth-order accurate central scheme was employed.

A more recent DNS of an incompressible jet in crossflow has been reported by Muppidi and Mahesh [10]. They considered injection of a round jet into a laminar boundary layer and included a round duct below the injection orifice in their simulation. As boundary condition for the jet, data obtained in a computation of fully developed pipe flow were used in this study.

With regard to compressible formulations for subsonic flow, simulations of the jet in crossflow have been presented, for example, by Guo et al. [11], Renze et al. [12] and Iourokina and Lele [13]. These three studies are all directed toward applications in film cooling of gas turbine blades. The jets investigated by Renze et al. [12] and Iourokina and Lele [13] were inclined toward the downstream direction.

Like the scalar field known from other configurations such as fully developed channel flow, for example, the scalar field of the jet in crossflow is characterized by a structure of well-mixed "plateaux" and steep cliffs, as has been discussed by Shan and Dimotakis [4].

Su and Mungal [5] have observed, for the round jet, a structure of fine filaments normal to the jet's trajectory, which they associate with instantaneous, known structures in the jet's wake (described, for example, by Fric and Roshko [1]).

The depth of penetration into the crossflow is strongly influenced by the ratio of the momentum fluxes of the jet and the crossstream, $J_I = (\rho_j u_j^2)/(\rho_{cf} u_{cf}^2)$. Furthermore, an influence of the jet's velocity profile (for example, parabolic, top-hat etc.) has been noted by New et al. [3]. Su and Mungal [5] have concluded that the velocity profile of the jet stream (at exit section) has greater impact onto the development of the scalar field than the momentum flux ratio J_I.

Trajectory behavior for an arrangement of round jets more or less closely spaced in the spanwise direction has been described in great detail by Kamotani and Greber [14]. They injected into a duct where there could be an influence because of the presence of an opposite (upper) duct wall on the flow field. With regard to the present work, which involves a ratio of the size of the injection orifice to total duct height that is still rather large, it appears worth noting that Kamotani and Greber [14] observed a comparatively large influence of this geometrical ratio onto the jet trajectory when the jet arrangement is to be considered two-dimensional.

As the above discussion shows, a large part of previous work on transverse injection into a crossflow is limited to incompressible or subsonic transverse jets without reaction. Nevertheless, some studies have also considered reacting transverse jets, such as those of Denev et al. [15, 16], who presented incompressible LES and DNS of a wall-normal, round jet in crossflow, including chemical reaction, performed using a finite volume formulation.

The present work extends the previous investigations by considering transverse injection of a reacting jet from a slot into fully developed turbulent channel flow. Furthermore, the slot is fully coupled with the channel domain, enabling flow interaction and allowing reactions to take place already within the transverse slot.

The paper is organized as follows: Section 2 discusses the flow configuration investigated, especially the geometrical and physical simplifications made. In Section 3, the mathematical model, the LES approach and computational details are presented. Section 4 describes selected results of instantaneous flow variables and statistical results. The latter cover the behavior of averaged primitive flow variables, Reynolds stresses and their transport, and the wall heat flux and the integrated heat release term. Effects of flow deceleration upstream of the jet and of flow acceleration near the upper wall are highlighted.

2. Flow configuration

The present work is directed toward transverse injection of a fuel jet into a subsonic crossflow of air and toward chemical reaction with heat release when the fuel and air streams mix, in order to show that LES of such a problem using methods of high order of accuracy is feasible. The simulation to be discussed subsequently is therefore based on a configuration that has been simplified both geometrically and physically.

A sketch of the geometrical configuration employed is displayed in Figure 1. Injection of the jet is performed through a narrow spanwise slot into a main channel with parallel walls, which have a distance of $2\,h_1$. The injected fluid is convected through a side channel of half width h_2, which is mounted perpendicularly to the main channel. Such a geometrical configuration will usually not be ideal for real combustion chambers, but is regarded here as a generic situation allowing easier numerical treatment and ensemble averaging along the span. In the present case, the ratio of channel half widths has been chosen to be $h_1/h_2 = 16$. The flow entering the main channel is a fully developed, turbulent channel flow

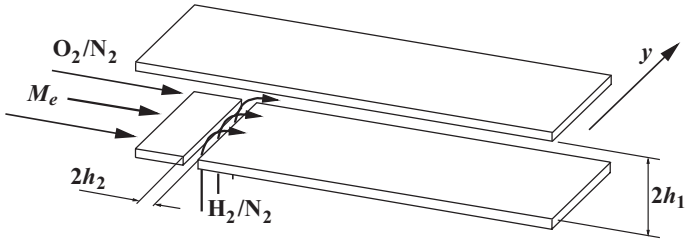

Figure 1. A schematic representation of the statistically two-dimensional model configuration considered. The jet consists of nitrogen with a small fraction of hydrogen and is transversely injected into turbulent channel flow consisting of air at an entrance Mach number M_e.

of air (assumed to be a mixture of oxygen and nitrogen with mass fractions of $Y_{O2} = 0.23$ and $Y_{N2} = 0.77$) at a bulk Mach number of 0.5, a bulk Reynolds number of 3000 (based on bulk mass flux, channel half width and viscosity at wall temperature) and a friction Reynolds number $Re_\tau = 198$. The walls of the present configuration are isothermal and are kept at a constant temperature, $T_w = 700$ K.

Through the spanwise slot, which is placed at a distance of approximately $4\,h_1$ downstream of the main channel inlet, a plane jet consisting of a mixture of hydrogen and nitrogen with mass fractions of $Y_{H2} = 0.016875$ and $Y_{N2} = 0.983125$ enters the crossflow. The ratios of incoming mass and momentum flux rates in the side or injection channel (IC) to the respective fluxes in the main or combustion channel (CC) are $J_M = 0.043$ and $J_I = 0.62$, respectively. These values of J_M and J_I are obtained through averaging at the inlets of main and side channels.

3. Simulation method

3.1. *Mathematical models*

The working gas is a mixture of N_s ideal gases, satisfying the equation of state $p = \rho RT$, where R is used to designate the gas constant of the mixture, T is the temperature and ρ, p are the sums of the N_s partial densities and pressures. The specific heats $C_{p,\alpha}$ and $C_{v,\alpha}$ of species α, as well as the ratios $\gamma_\alpha = C_{p,\alpha}/C_{v,\alpha}$ depend on temperature T. For the present study, the approximation

$$C_{p,\alpha} = \frac{\mathcal{R}}{W_\alpha}(a_{1,\alpha} + a_{2,\alpha}T + a_{3,\alpha}T^2 + a_{4,\alpha}T^3 + a_{5,\alpha}T^4), \tag{1}$$

[17] is assumed to hold, $\mathcal{R}$ denoting the universal gas constant, and W_α being the molecular weight of each component. Regarding the coefficients $a_{i,\alpha}$, two temperature regimes, $T \leq 1000$ K and $T > 1000$ K, are distinguished, as also done by Mahle [18] for LES of plane reacting mixing layers.

The flow is governed by the transport equations for mass, momentum and total energy of a compressible reacting gas mixture formulated in Cartesian coordinates,

$$\frac{\partial \rho}{\partial t} = -\frac{\partial(\rho u_j)}{\partial x_j},$$

$$\frac{\partial(\rho u_i)}{\partial t} = -\frac{\partial}{\partial x_j}(\rho u_j u_i) - \frac{\partial p}{\partial x_i} + \frac{\partial \tau_{ij}}{\partial x_j} + f_{V,i},$$

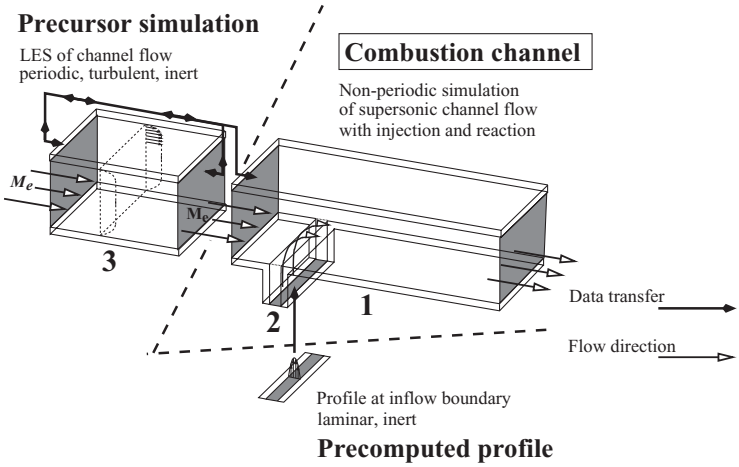

Figure 2. The structure of the simulation, schematically depicted, involving three coupled grid blocks 1, 2 (together forming the combustion channel) and 3 (for carrying out a simultaneous precursor LES). For laminar inflow of fuel gas into the side channel, the inlet profile may be determined previously, as shown.

$$\frac{\partial(\rho E)}{\partial t} = -\frac{\partial}{\partial x_j}(\rho u_j E) + \frac{\partial}{\partial x_j}(u_i \tau_{ij}) - \frac{\partial}{\partial x_j}(p u_j) + u_i f_{V,i} + \underbrace{\frac{\partial}{\partial x_j}(\lambda \frac{\partial T}{\partial x_j}) - \frac{\partial}{\partial x_j}\left(\rho \sum_{\alpha=1}^{N_s} h_{s,\alpha} Y_\alpha V_{\alpha,j}\right)}_{= -\frac{\partial q_j}{\partial x_j}} - \sum_{\alpha=1}^{N_s} \Delta h^0_{f,\alpha} \omega_\alpha. \tag{2}$$

Velocity components, total energy, viscous stress components, molecular heat flux components, mass production rate and standard enthalpy of formation for each species α are denoted by u_i, E, τ_{ij}, q_j, and ω_α, $\Delta h^0_{f,\alpha}$, respectively. $f_{V,i}$ represents a body force which is necessary to overcome wall friction in the simulation of fully developed channel flow. Such a flow is computed in a precursor simulation and provides inflow conditions for the jet in crossflow configuration sketched in Figure 1.

While the mass production rates ω_α are zero in the precursor simulation, the body force $f_{V,i}$ vanishes in CC and IC (blocks 1 and 2, see Figure 2). Presently, it is assumed that the combustion of hydrogen (fuel F) with oxygen (oxidizer O) in the CC may be described by a one-step, infinitely fast and irreversible reaction $2\,H_2 + O_2 \rightarrow 2\,H_2O$. In block 1, $N_s = 4$ gas components (H_2, O_2, H_2O and N_2) are taken into account – intermediate reaction products do not appear.

In order to describe the transport of gas components, a mixture fraction approach is chosen. The mixture fraction $0 \leq \xi \leq 1$ is defined as

$$\xi = \frac{s_R Y_F - Y_O + Y_{O,o}}{s_R Y_{F,f} + Y_{O,o}} \quad \text{with} \quad s_R = \frac{\nu'_O W_O}{\nu'_F W_F}. \tag{3}$$

Here, Y_O and Y_F are used to designate the mass fractions of oxidizer and fuel, respectively. $Y_{F,f}$ and $Y_{O,o}$ denote the mass fractions in the pure jet or crossflow fluids, ν'_F and ν'_O denote the corresponding stoichiometric coefficients and W_F and W_O denote the corresponding molar masses.

ξ is a passive scalar and its evolution is governed by the relation

$$\frac{\partial(\rho\xi)}{\partial t} = -\frac{\partial}{\partial x_j}(\rho u_j \xi) + \frac{\partial}{\partial x_j}\left(\frac{\mu}{Sc}\frac{\partial \xi}{\partial x_j}\right). \tag{4}$$

Inherent to the concept of a mixture fraction ξ is the use of constant Schmidt numbers $Sc = \mu/(\rho D)$ for all species. In this study, $Sc = 0.7$, where D is the diffusion coefficient of any of the species in the mixture. From $\xi(\vec{x}, t)$, the structure of the flame can be determined.

The flame is assumed to be locally one-dimensional and thin compared to the scales of turbulence. Mass fractions of given components α are functions of the mixture fraction ξ only, $Y_\alpha = \rho_\alpha/\rho = Y_\alpha(\xi)$. The link between Y_α and ξ is provided by the classical, piecewise linear Burke–Schumann relations, as described by Poinsot and Veynante [19], for example, with a slight hyperbolic tangent smoothing around ξ_s [20] being added to avoid a zero chemical source term, resulting from piecewise linear relations. Then, in Equation (2), the mass production rate may be written as

$$\omega_\alpha = -\chi \frac{d^2 Y_\alpha}{d\xi^2}, \quad \text{wherein} \quad \chi = \rho D\left(\frac{\partial \xi}{\partial x_i}\frac{\partial \xi}{\partial x_i}\right) \tag{5}$$

is the scalar dissipation rate [21]. In the present case, using the Burke–Schumann relations, ω_α is zero unless ξ corresponds to the stoichiometric mixture fraction ξ_s, where it becomes infinity:

$$\omega_\alpha = -\chi \frac{Y_{F,f}}{1-\xi_s} \cdot \delta(\xi - \xi_s) = -\chi \frac{d}{d\xi}\int \frac{Y_{F,f}}{1-\xi_s} \cdot \delta(\xi - \xi_s)\, d\xi. \tag{6}$$

As usual, we use the definition

$$\tau_{ij} = 2\mu S_{ij} + \left(\mu_d - \frac{2}{3}\mu\right) S_{kk}\delta_{ij} \tag{7}$$

for viscous stresses in Equation (2), where μ and μ_d denote the shear and bulk viscosities, respectively, and S_{ij} is the deformation tensor. Using Fick's law, we simplify the diffusion flux

$$\rho Y_\alpha V_{\alpha,j} = -\rho D_\alpha \frac{\partial Y_\alpha}{\partial x_j} \approx -\frac{\mu}{Sc}\frac{dY_\alpha}{d\xi}\frac{\partial \xi}{\partial x_j}, \qquad Sc = \frac{\mu}{\rho D} \tag{8}$$

for a species α along direction x_j, $V_{\alpha,j}$ being the diffusion velocity of species α. To simplify the setting, thermodiffusion and barodiffusion are neglected here. The molecular transport coefficients for the gas mixture are computed efficiently and accurately using the programme EGLiB, which is based on kinetic theory of gases (see [22]). While the transport Equations (2) are integrated in time, the temperature T has to be determined from the definition of the total energy E before each time step. In the present approach, this is

accomplished by solving a nonlinear fifth-order equation in T iteratively, using the Brent algorithm, as described in [23].

3.2. *Semi-implicit LES approach*

For an LES, the set of Equations (2) has to be low-pass filtered in space. In order to avoid (explicit) modelling of each filtered nonlinear term, we perform explicit filtering of the equations (except for the heat release term) at each time step with a composite filter, as suggested by Mathew et al. [24] and call it the implicit LES part. Q_N is, for instance, for the periodic direction, the approximate inverse of the sixth-order one-parametric Padé filter, G [25]. More details on explicit filtering applied to the case of a reacting jet in supersonic crossflow can be found in [26]. The low-pass filtered heat release term

$$\bar{\omega} = -\sum_{\alpha=1}^{4} \Delta h^0_{f,\alpha} \bar{\omega}_\alpha \tag{9}$$

in the energy equation requires explicit modelling. We use a model that is the LES equivalent of the statistical model derived by Bilger [27], and will be briefly sketched in the following. For more details, see also [18]. First, we make use of the definition of the heat release term

$$q^0 = -\sum_{\alpha} \Delta h^0_{f,\alpha} W_\alpha (\nu''_\alpha - \nu'_\alpha), \tag{10}$$

where ν'_α and ν''_α are the stoichiometric coefficients of reactants and products, respectively. The reaction rate of the global step (identical for all species) is

$$\omega_G = \frac{\omega_\alpha}{W_\alpha(\nu''_\alpha - \nu'_\alpha)}, \tag{11}$$

and the heat release per unit volume and unit time that is obtained is

$$q^0 \omega_G = -\sum_{\alpha} \Delta h^0_{f,\alpha} \omega_\alpha. \tag{12}$$

Combining Equation (6), which gives ω_α, with the above equations and filtering yields

$$\bar{\omega} = \frac{q^0 Y_{F,f}}{W_F \nu'_F (1-\xi_s)} \int\int \chi' \delta(\xi' - \xi_s) \tilde{F}_{\chi\xi}(\chi', \xi')\, d\chi' d\xi'. \tag{13}$$

In Equation (13), $\tilde{F}_{\chi\xi}(\chi, \xi)$ denotes a two-dimensional filtered density function, which is related to the conditionally filtered scalar dissipation rate $\tilde{\chi}_\xi$ and a filtered density function $\tilde{F}_\xi$ for the mixture fraction ξ through

$$\tilde{F}_{\chi\xi}(\chi, \xi) = \tilde{F}_{\chi|\xi}(\chi|\xi = \xi') \cdot \tilde{F}_\xi(\xi) \tag{14}$$

and

$$\tilde{\chi}_\xi(\xi') = \int_0^\infty \chi' \tilde{F}_{\chi|\xi}(\chi'|\xi = \xi') d\chi'. \tag{15}$$

Inserting this into $\bar{\omega}$ leads to

$$\bar{\omega} = \frac{q^0 Y_{F,f}}{W_F \nu_F'(1-\xi_s)} \tilde{F}_\xi(\xi_s) \int \chi' \tilde{F}_{\chi|\xi}(\chi|\xi=\xi')\, d\chi' = 2\, Q_e \cdot \tilde{F}_\xi(\xi_s) \cdot \tilde{\chi}_\xi(\xi_s), \tag{16}$$

thus defining the heat release parameter Q_e. To obtain the model that we use for the filtered heat release, the conditionally filtered scalar dissipation rate $\tilde{\chi}_\xi$ and the filtered density function $\tilde{F}_\xi$ of the mixture fraction are replaced in the preceding equation by modelled terms $\tilde{\chi}_\xi^m$ and $\tilde{F}_\xi^m$. The fdf $\tilde{F}_\xi$ is presently modelled by a beta function that involves the filtered mixture fraction $\tilde{\xi}$, available from its filtered transport Equation (4), and the sub-grid variance of the mixture fraction,

$$(\xi^2)_{sg} = \widetilde{\xi^2} - (\tilde{\xi})^2, \tag{17}$$

for which a gradient model is used. Further, $\tilde{\chi}_\xi^m$ is obtained using a form function and a gradient model for the unresolved part of the scalar dissipation as well.

The code employed for the present LES of transverse injection into subsonic channel flow enables the use of artificial viscosities μ^a and μ_d^a, artificial heat conductivity λ^a and artificial diffusion coefficients χ_ξ (see [26] for details and references). For the simulation described in the following, μ^a, μ_d^a and χ_ξ are zero, while λ^a does not vanish. The concept of artificial molecular transport coefficients helps to reduce oscillations in the solution when there are gradients present in the flow, which cannot be resolved on the grid. Presently, the coefficient C_λ^a varies between 0.005 and 0.02.

3.3. *Computational details*

The low-pass filtered transport Equations (2) and (4) are discretized in space using sixth-order compact central schemes [25] and an explicit fourth-order Runge–Kutta time-integration scheme [28]. The computational grid used is in particular refined in the region of the spanwise slot in the main (axial) flow direction as well as near to the CC's walls in the direction normal to these. Table 1 gives the dimensions of grid blocks, while Table 2 contains the number of grid points in each block.

At walls (of CC and IC) no-slip and impermeability conditions are imposed. Walls are isothermal and non-catalytic, which means that rates of reaction vanish. Thus, wall-normal

Table 1. Dimensions of three grid blocks in multiples of wall units obtained for the LES of a fully developed turbulent channel flow in block 3, along with the positions of the slot center (x_{sc}) and of the left and right slot edges (x_{sL} and x_{sR}), measured from the inflow plane of block 1 and normalized in the same manner.

	Block 1	Block 2	Block 3
L_x^+	2503.4	417.1	3690.9
$L_y^+ = 4\pi h_1^+/3$	837.5	837.5	837.5
$L_z^+ = 2\,h^+$	399.9	25.0	399.9
h^+	199.9	12.5	199.9
x_{sc}^+	825.2		
x_{sL}^+	812.3		
x_{sR}^+	837.3		

Table 2. Number of grid points in each block and number of processors used.

	n_x	n_y	n_z
Block 1	512	64	128
Block 2	128	64	32
Block 3	160	64	128
Total number of grid points			5.76×10^6
Total number of CPUs			44

diffusion fluxes disappear in wall grid points, e.g., the wall-normal flux of ξ. Inflow and outflow boundary conditions are based on a characteristic decomposition of transport equations (see [18, 29]).

Sudden changes in the domain boundary's geometry, such as the sharp edges where IC and CC meet, may lead to singularities appearing in the exact flow field and to additional errors when the equation system is solved numerically (see, for example, [30, 31]). As a consequence, the flow variables are filtered in a small neighborhood of each side channel edge in order to control spurious oscillations, which possibly occur at those edges. An explicit filter of Gaussian-type having a width of $4\Delta x$ is utilized.

Initial conditions for the CC and IC (blocks 1 and 2) are obtained from a separate Reynolds-Averaged Navier–Stokes (RANS) simulation with a (k, ε)-turbulence model, neglecting chemical reaction. Near the inlet of the CC, fluctuations taken from fully developed channel flow (block 3) are superimposed on the statistical steady state solution by means of a hyperbolic tangent weighting.

During the LES performed on the SGI Altix 4700 supercomputer of the Bavarian Academy of Sciences, a total of about 6,50,000 time steps have been computed. This includes about 4,50,000 time steps prior to statistical evaluation and excludes computational time needed to establish a proper inflow condition. The simulation used more than 2650 hours of wall clock time.

4. Results

We start the discussion of results with instantaneous views of jet in subsonic crossflow. The instantaneous flow variables shown are $(Q_N \star G)^2-$filtered quantities, which, in order to simplify the notation, do not carry an overbar or a tilde. The overbar and the tilde are later needed to denote Reynolds and Favre averages, $\bar{a}$ and $\tilde{a}$, respectively. The corresponding fluctuations are a' and a'', respectively.

4.1. *Instantaneous flow variables*

It is instructive to have a look at the flow field in the complete computational domain first, before we show details in the neighborhood of the injection zone. Figure 3 contains snapshots of the local Mach number, $M = \sqrt{u_i^2}/c$, and the temperature T. It can be clearly seen that the reacting jet accelerates the flow in the channel, although it is injected perpendicularly to the main stream and the mean ratio of injected to upstream momentum flux (averaged over the corresponding cross-sections) is rather low ($J_I \approx 0.62$). The flow downstream of the injection slot reaches local Mach numbers close to 0.85. The locally strong increase in temperature in the jet and in the developing mixing layer is not fully realistic because we use infinitely fast chemistry. Nevertheless, the fact that the flow separates locally and

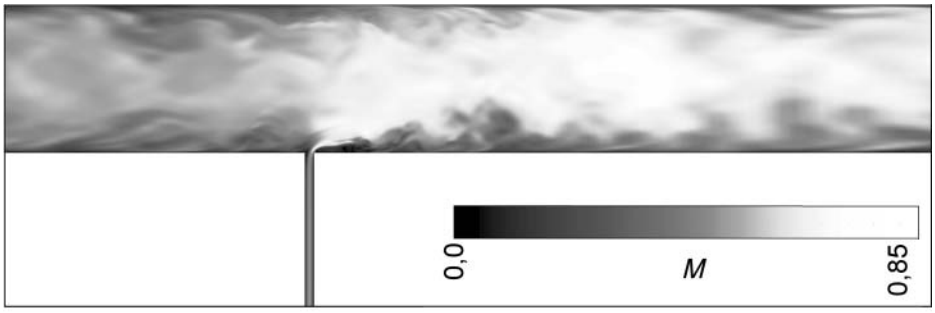

(a) Local Mach number

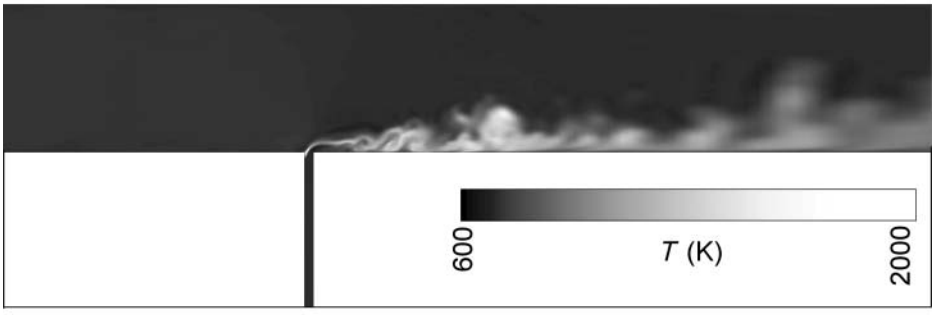

(b) Temperature

Figure 3. Snapshots of (a) the local Mach number, and (b) the temperature in the vertical midplane of the complete computational domain.

instantaneously on the left wall of the side-channel (indicated by high temperature there) is certainly independent of whether detailed or fast chemistry is used. It indicates that the flow in the IC has to be computed simultaneously with the flow in the main channel. A specification of boundary conditions in the plane of intersection of both channels is not appropriate.

Figure 4 contains two successive snapshots of the local Mach number in the neighborhood of the side-channel as carpet plots, together with contour lines for $M = 0.1$, 0.3 (in white) and 0.6 (in black). Islands of low Mach number flow ($M = 0.3$) have left the recirculation zone downstream of the injection slot and are washed away. The deformation and transport of large-scale structures with Mach numbers between 0.3 and 0.6 can also

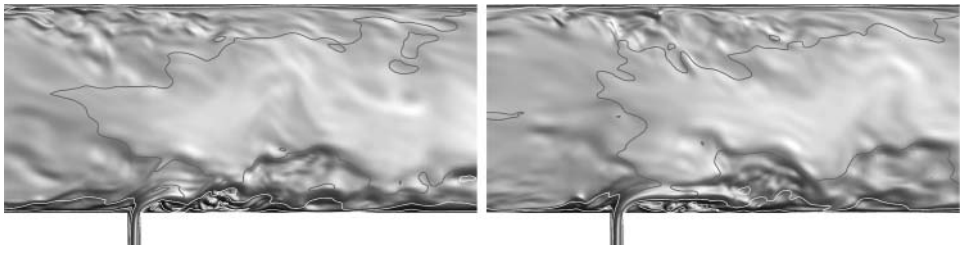

Figure 4. Carpet plots and contour lines of local Mach number at two successive instants of time. Time difference: $\Delta t = 13.2\, h_2/u_{m,in,1}$. The meaning of the contour lines is described in the discussion of simulation results in Section 4.1.

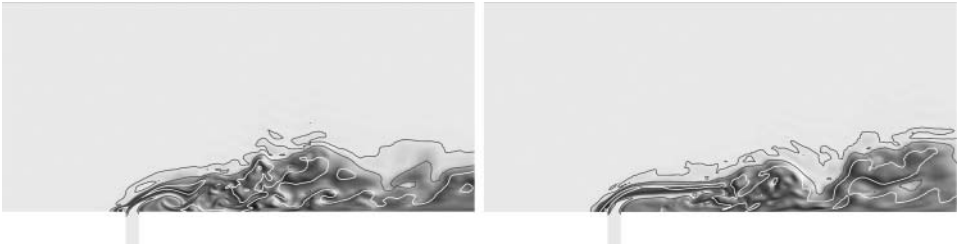

Figure 5. Carpet plots and contour lines of water vapor concentration Y_{H2O} at two successive instants of time. Time difference: $\Delta t = 13.2\, h_2/u_{m,in,1}$. The meaning of the contour lines is described in the discussion of simulation results in Section 4.1.

be observed in the lower part of the channel. Water vapor is the end product of the global reaction assumed. Its concentration is displayed in Figure 5 in the same plane and at the same instants of time as chosen in Figure 4. As the contour lines of the H_2O mass fraction with values of 0.001, 0.01 (in black) and 0.05 (in white) show, chemical reaction already takes place on the upstream (windward) side of the jet where oxygen and hydrogen first get together. Figure 5 also shows that water vapor occasionally enters the IC as a result of separation of jet before it reaches the sharp upstream edge. The stoichiometric mixture fraction $\xi_s \approx 0.632$ is used in Figure 6 to illustrate contours of the flame front together with temperature and water vapor fields in planes parallel to the lower wall at a distance of $\Delta z^+ = 2$. It is interesting to see that on the windward side of the jet, the flame front (black line) forms pockets in which unburned jet fluid resides. In the lower part of Figure 6 this is indicated by spots of low temperature (the jet fluid has a temperature of 700 K) and in the upper part by patches of zero water vapor concentration. Comparing projections of instantaneous velocity vectors into vertical y- and z-planes taken from any x-position of the fully developed channel flow with those from the midplane of the side-channel in Figure 7 provides an impression of the complexity and intensity of turbulent mixing processes that take place in the mixing layer between jet and crossflow. At $(x - x_{sc})/h_2 = 0$ and close to the intersection between main and side-channel, the velocity vectors are practically parallel, which is due to the fact that the injected jet is still in a state of laminar flow there. Near the upper wall, the vectors indicate local streamwise vortices, which seem to be more vigorous than those far upstream. The reason for this is that the flow is accelerated near the upper wall. A confirmation of this conjecture will be given later when profiles of the Reynolds stresses in spanwise and wall-normal directions are discussed.

4.2. *Statistically averaged primitive flow variables*

Snapshots of LES variables are fascinating and can be very instructive; however, they are perhaps not of great benefit for engineers who search for data they can use for comparison with their RANS results. We therefore focus on the behavior of mean flow variables now, as obtained from averaging in spanwise flow direction and in time, and turn later to a discussion of Reynolds stresses and their variations because of jet in crossflow. In what follows, mean flow variables are presented in terms of wall-normal profiles at selected x-positions. We start the discussion with the mean velocity field. Figure 8 shows profiles of the mean streamwise velocity $\bar{u}$, normalized with the bulk velocity at inflow $u_{m,in,1}$ at selected positions (the axial coordinate x_{sc} corresponds to the axial position of the side channel centerline, this position being measured from the upstream inlet plane of the main channel, i.e., from the beginning

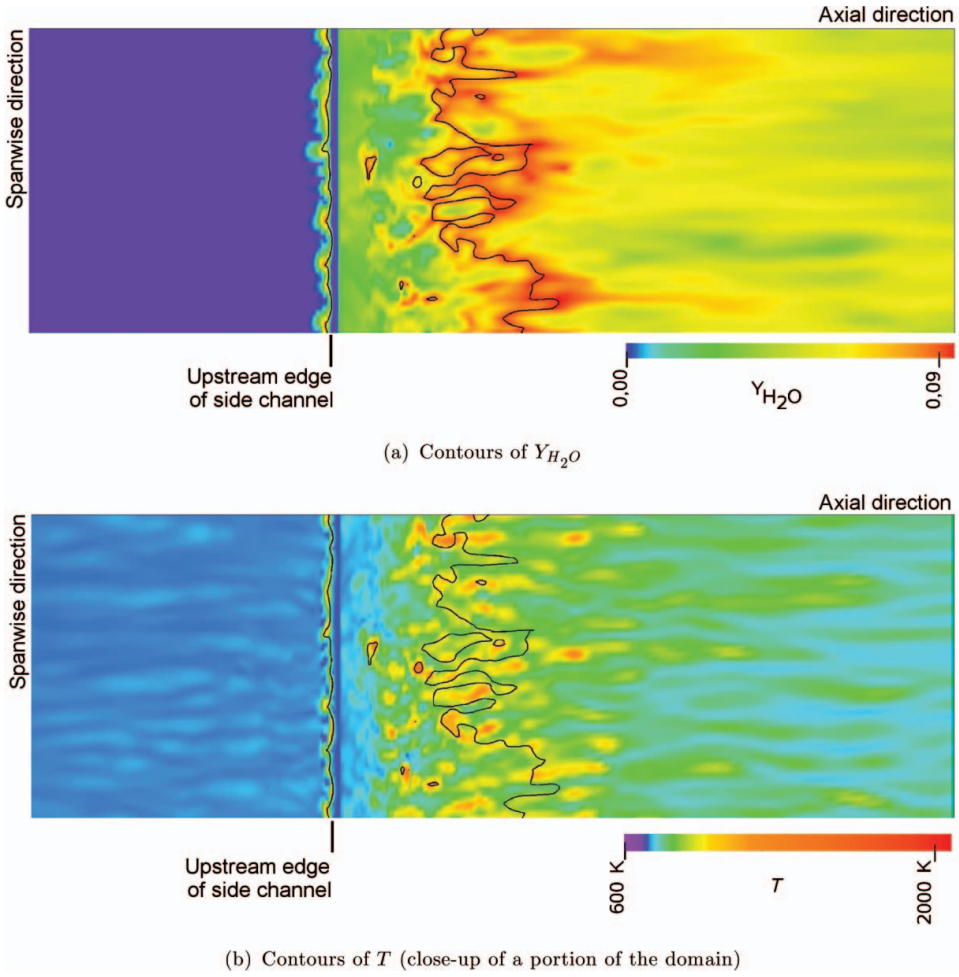

Figure 6. Contours of the flame front illustrated by the stoichiometric mixture fraction together with contours of water vapor concentration and temperature, respectively, at a distance from the lower wall of $\Delta z^+ = 2$ and at the same instant.

of the domain). Two of these profiles are displayed in color, because these represent planes of special interest. The **blue** profile corresponds to an x-position $(x - x_{sc})/h_2 = -3$, which is one entire side channel width, $2\,h_2$, upstream of the side-channel's windward edge. The **red** profile is located at $(x - x_{sc})/h_2 = 9$ (corresponding to a position of $0.5\,h_1$ downstream of the side channel's leeward edge) and hence crosses the mixing layer where the turbulence production is at maximum level. The black solid profile corresponds to the fully developed turbulent channel flow at the inlet. At $(x - x_{sc})/h_2 = -3$, the flow is decelerated in the lowest quarter, $z/h_1 < 0.5$, compared with the incoming flow and accelerated in the upper three quarters. It cannot be seen in this plot, but in the enlarged plot of Figure 9, that a tiny recirculation zone exists in front of the jet. Its vertical extension is $0.16\,h_2$. The zone of mean reversed flow downstream of the slot (red curve) has a height close to the width of the side-channel, $1.4\,h_2$. The maximum upstream velocity is 30% of the bulk velocity at inflow. In view of a later discussion of Reynolds stress production, we note

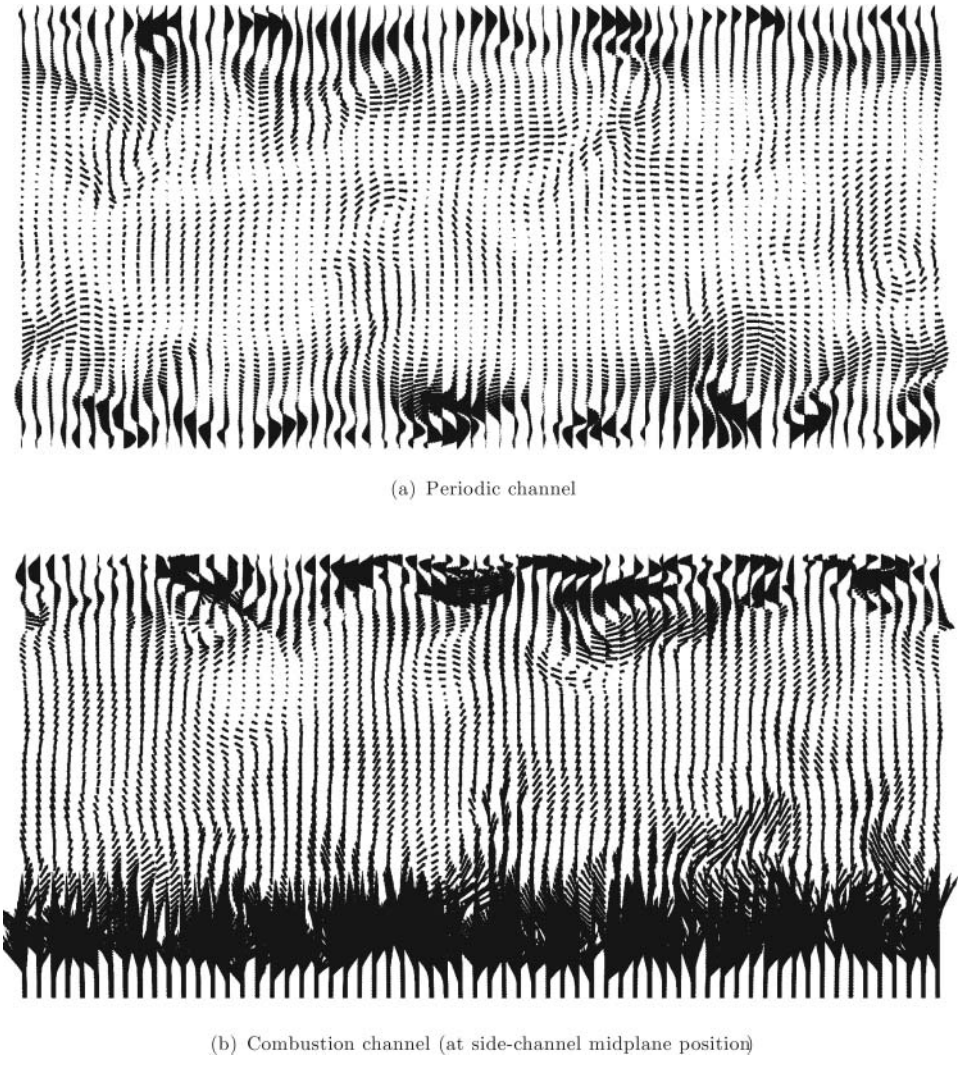

Figure 7. Projections of velocity vectors into spanwise planes of (a) periodic channel, and (b) combustion channel at $(x - x_{sc})/h_2 = 0$ (midplane of the side-channel). Equal scaling of vector length.

a strong increase in the mean velocity gradient at $z/h_1 \approx 0.15$ compared with that at the same position far upstream. Contours of the mean wall-normal velocity, normalized the same way as the streamwise velocity, are shown in Figure 10. The jet penetrates deeply into the channel so that at its center the mean vertical velocity is still 10% of the bulk velocity far upstream. One channel half width h_1 downstream of the slot, the mean flow is directed toward the lower wall and reattaches after having formed an elongated recirculation zone, which is tilted toward the wall at its downstream end. As a result of this inclination, the red profile in Figure 11 first indicates upward flow (with negative $\bar{u}$) and then downward flow (with positive $\bar{u}$) before, at larger distance from the wall, only positive values of $\bar{w}$ are observed. Figure 12 presents profiles of the normalized mean density and

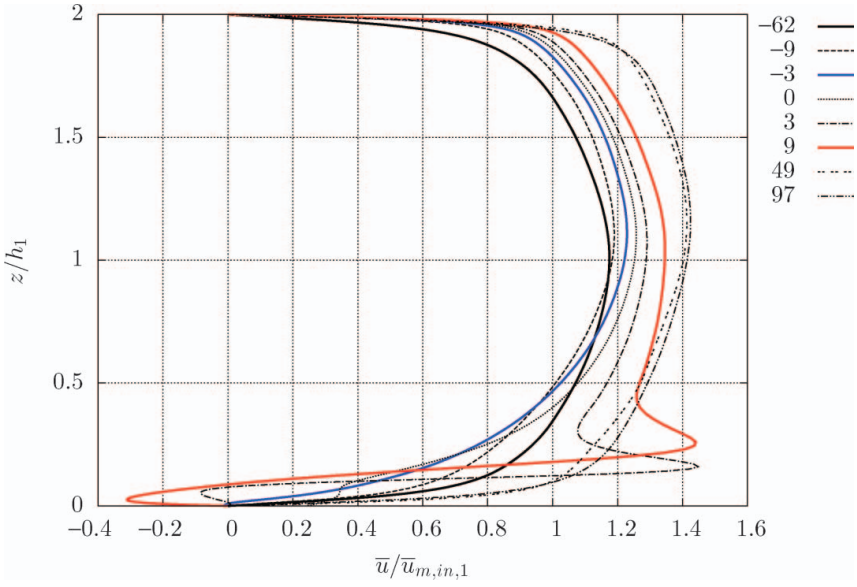

Figure 8. Profiles of normalized mean streamwise velocity at selected positions $(x - x_{sc})/h_2$.

gives the rough impression that it is reduced not only within the jet and its downstream recirculation zone but also in the small recirculation zone upstream of the slot. To understand the density variations more clearly, it is useful to express the density as a function of pressure p, entropy s and species mass fractions Y_α and to write down its mean streamwise

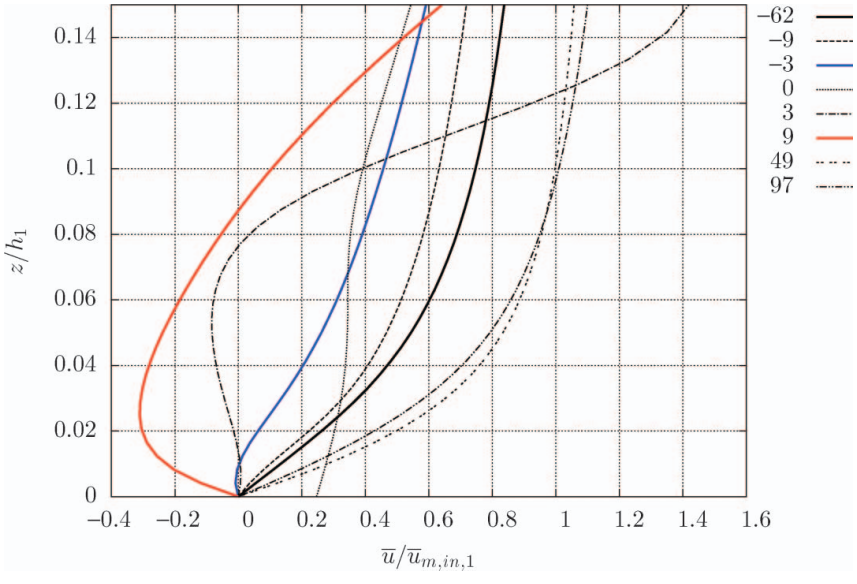

Figure 9. Zoom into profiles of figure 8. Symbols as in Figure 8.

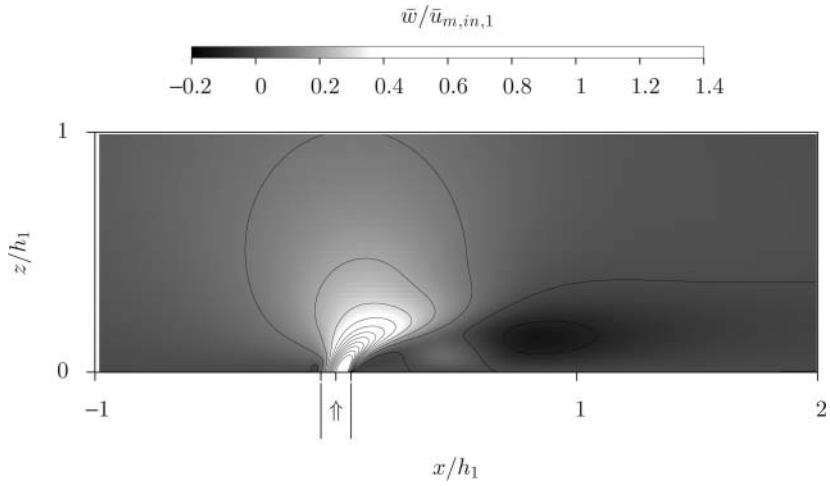

Figure 10. Mean wall-normal velocity normalized with bulk velocity at inflow lower half of the channel. The constant difference between values of isolines is 0.1.

gradient:

$$\frac{\partial \bar{\rho}}{\partial x} \approx \frac{1}{\bar{c}^2}\frac{\partial \bar{p}}{\partial x} + \frac{1}{c_p \bar{T}}\left(\bar{\rho}\sum_{\alpha}\bar{h}_{\alpha}\frac{\partial \bar{Y}_{\alpha}}{\partial x}\right) + \text{h.o.t.} \tag{18}$$

Term in parenthesis approximates the mean heat release term. Correlations and terms responsible for mean entropy changes are summarized in higher order terms (h.o.t.). Starting

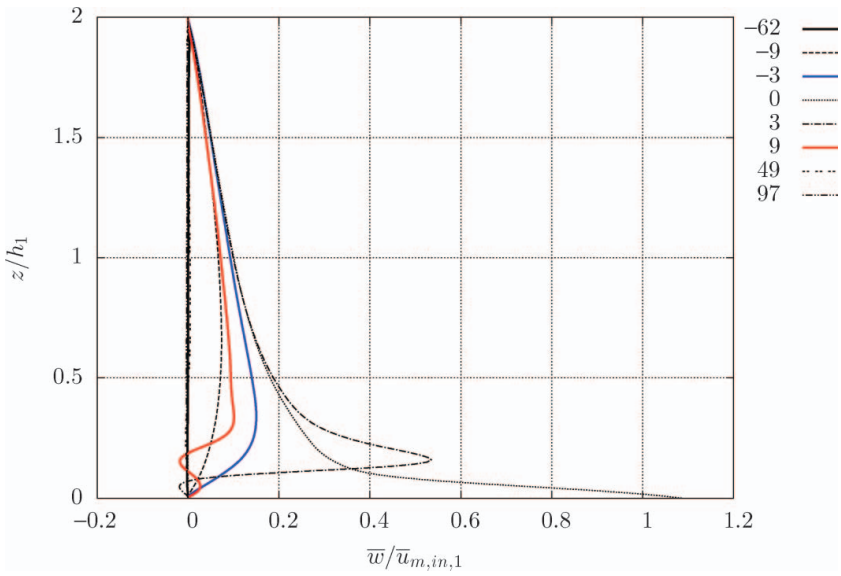

Figure 11. Profiles of normalized mean wall-normal velocity at selected positions $(x - x_{sc})/h_2$. Symbols as in Figure 8.

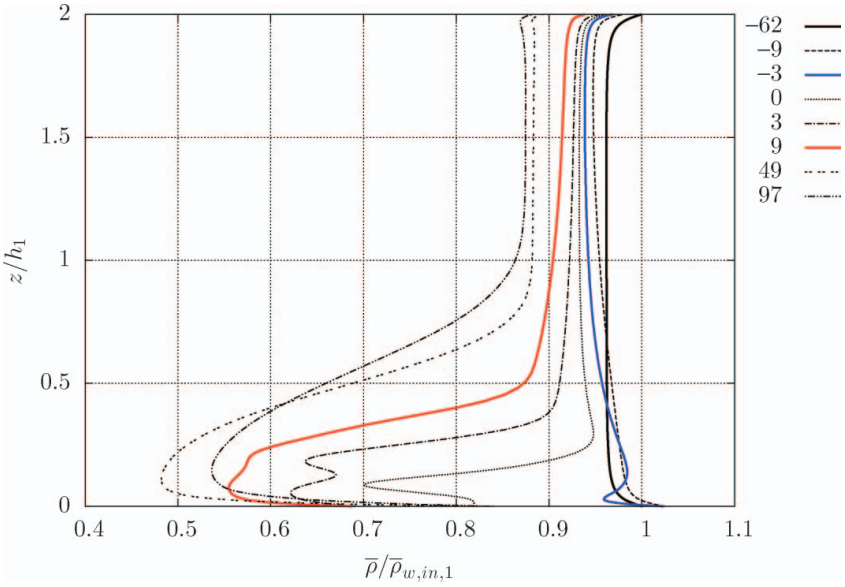

Figure 12. Profiles of normalized mean density at selected positions $(x - x_{sc})/h_2$. The blue and red profiles correspond to positions slightly upstream of the jet and in the middle of the downstream recirculation zone.

the discussion at the upper wall in Figure 12, both blue and red profiles indicate reduced mean density because of flow acceleration, since there is no heat release. This behavior persists over nearly 75% of the channel width until heat release provides a further reduction of density in the plane $(x - x_{sc})/h_2 = 9$, but an increase because of flow deceleration at $(x - x_{sc})/h_2 = -3$ for $z/h_1 < 0.4$ (also compare the blue pressure curve in Figure 14). Close to the wall ($z/h_1 \approx 0.025$, blue curve), heat release dominates over the compression effect and reduces the density below values that are typical for inert fully developed subsonic

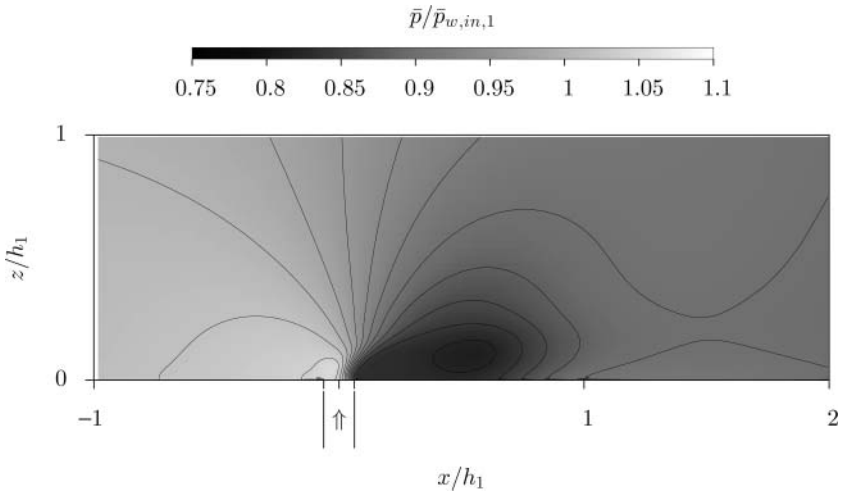

Figure 13. Mean pressure normalized with wall pressure at inflow. Lower half of channel. The constant difference between values of isolines is 0.02.

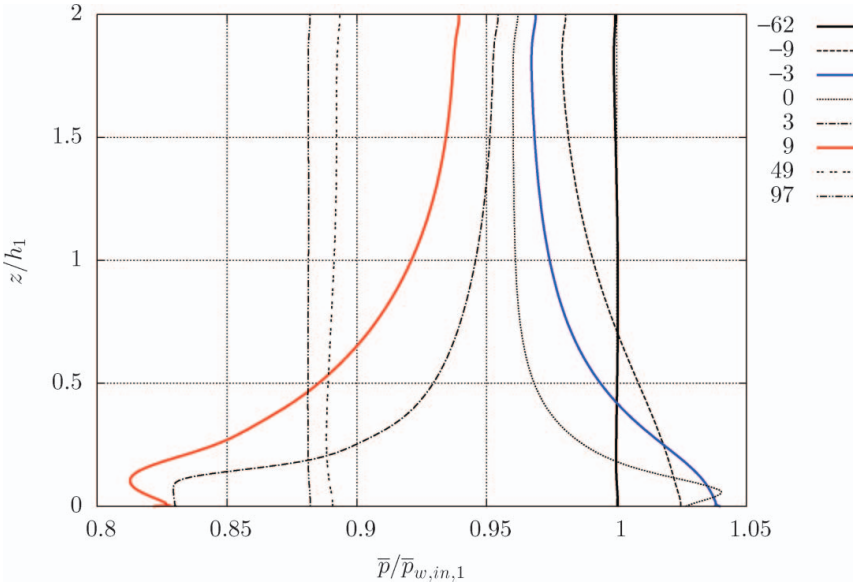

Figure 14. Profiles of normalized mean pressure at selected positions $(x - x_{sc})/h_2$. Symbols as in Figure 8.

channel flow (solid black curve). This is also supported by the peak in the mean temperature profile in Figure 15.

The contour plot of the normalized mean pressure with its contour lines (Figure 13) shows an extended zone of reduced pressure downstream of the slot, which seems to reflect a footprint of vortical motion in the recirculation zone. In fact the pressure minimum on the red profile (Figure 14) is at $z/h_1 \approx 0.1$. This is exactly the point where both velocity

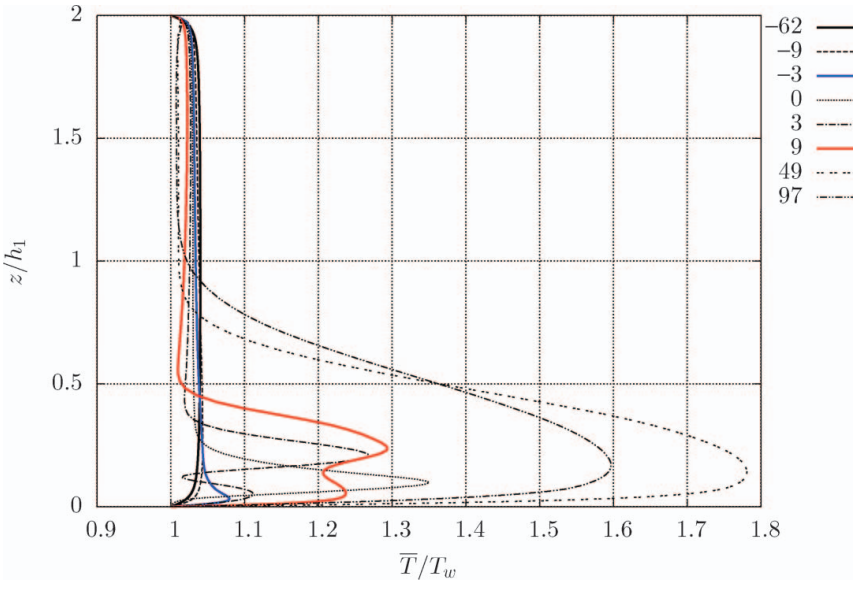

Figure 15. Profiles of normalized mean temperature at selected positions $(x - x_{sc})/h_2$. Symbols as in Figure 8.

components are very close to zero (eye of the vortex). There is also a region of pressure increase in front of the jet (Figures 13 and 14, blue curve). In order to understand the mechanisms that lead to this increase, one must keep in mind that the pressure and its streamwise gradient play a double role. From a hydrodynamic point of view, the pressure gradient is controlled by the velocity field and indicates flow acceleration/retardation. From

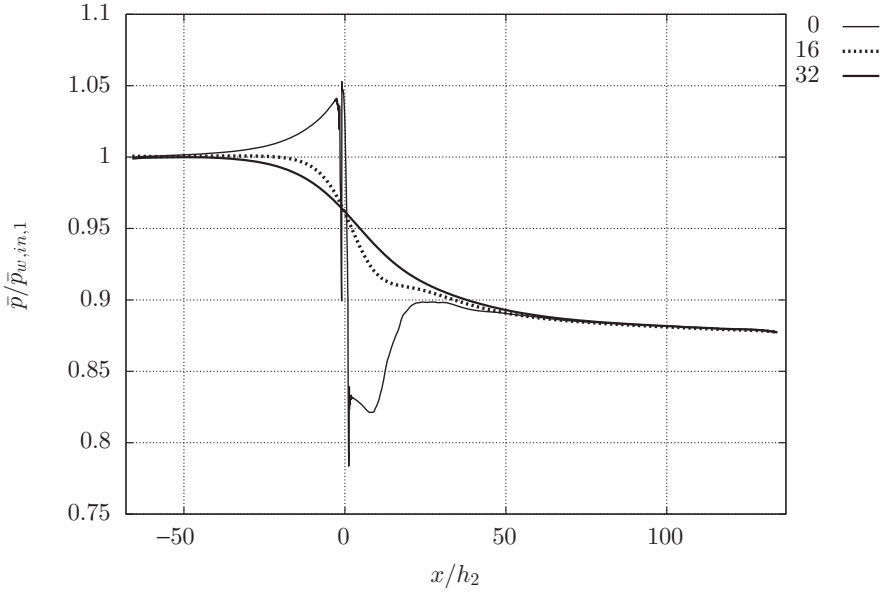

(a) Complete domain

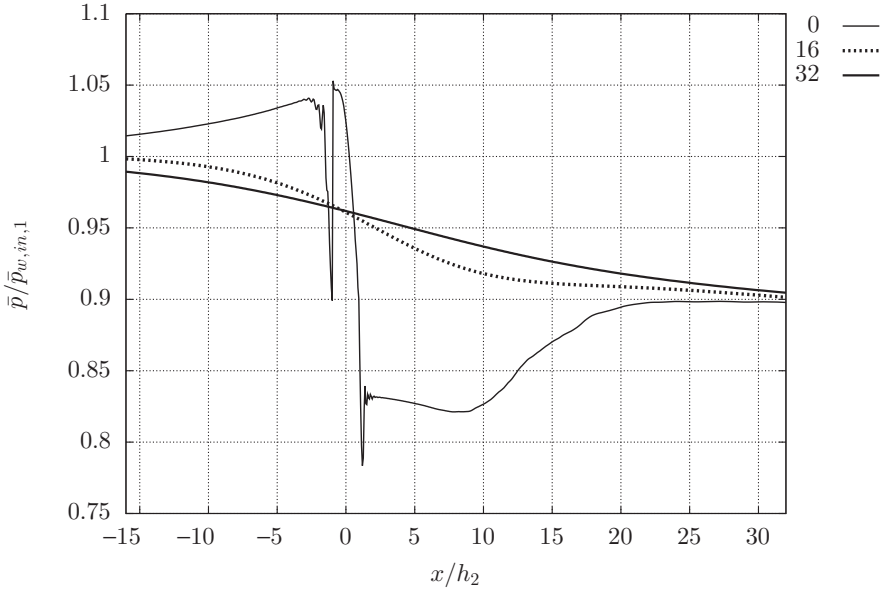

(b) Close-up

Figure 16. Streamwise distribution of mean pressure along both walls ($z/h_2 = 0, 32$) and in the midplane ($z/h_2 = 16$). Top: Complete domain. Bottom: Stretched x-coordinate.

a thermodynamic or kinetic theory of gases point of view, it is proportional to the gradient of mean kinetic energy of the translational degrees of freedom of gas molecules, which is the temperature gradient. In front of the jet, at $z/h_1 \approx 0.15$ (Figure 14, blue curve), the pressure increase is certainly a result of flow deceleration (compression) and weak temperature increase. At $z/h_1 \approx 0.025$, where the temperature peaks and the density is minimum, the thermodynamic part of the pressure does not really seem to contribute. In the upper half of the channel, where there is no heat release, the reduced pressure level is purely due to flow acceleration (blue and red curves of Figure 14). Profiles of mean temperature, normalized with the constant wall temperature, in Figure 15 confirm increase in temperature on the windward side of the jet and along its downstream development. Profiles downstream of the slot (at $(x - x_{sc})/h_2 = 3$ and 9) show double peaks, one close to the wall, i.e., in the recirculation region, and the other above the shear layer. The latter already reflect effects of heat release. As we follow the flow downstream, the released heat accumulates and leads to mean temperatures above $1.7\,T_w$ at $(x - x_{sc})/h_2 = 49$. At $(x - x_{sc})/h_2 = 97$, the peak temperature is already reduced, since the amount of heat release has gone down (see Section 4.5).

To conclude this section, we present the streamwise development of mean pressure along both walls and midplane ($z/h_1 = 1$) in Figure 16. Along the lower wall we observe the pressure increase in front of the jet, already discussed above and an overall pressure drop across the slot. As the sharp edge of the side-channel is approached from left, the pressure drops rapidly because of local expansion (see the bottom plot) in order to rise again steeply toward the center of the jet. The right edge of the side-channel experiences a further pressure rise. Downstream of position $(x - x_{sc})/h_2 = 9$, the pressure increases again until the jet reattaches along the lower wall near $(x - x_{sc})/h_2 \approx 16.5$. As to be expected, the mean pressure drops smoothly from the entrance to the outlet in the channel midplane and along the upper wall. The upper plot also confirms that the inflow plane is far enough upstream of the injection region.

4.3. *Reynolds stresses and their transport*

Given the mean pressure variations along the walls and the midplane of the main channel, we can already expect that the Reynolds stresses and their production will respond to changes of the mean shear rate and the presence of extra rates of mean strain. Parallel to these effects, there will be changes in the redistribution mechanism so that considerable modifications of the Reynolds stress anisotropy will result. With the help of the Reynolds stress balances, these mechanisms can be substantiated.

In Cartesian coordinates the stress balances read as follows:

$$\begin{aligned}
\frac{\partial}{\partial t}(\overline{\rho u''u''}) = {} & \underbrace{-\frac{\partial}{\partial x}(\tilde{u}\,\overline{\rho u''u''}) - \frac{\partial}{\partial z}(\tilde{w}\,\overline{\rho u''u''})}_{MT_{xx}} \quad \underbrace{-2\,\overline{\rho u''u''}\,\frac{\partial \tilde{u}}{\partial x} - 2\,\overline{\rho u''w''}\,\frac{\partial \tilde{u}}{\partial z}}_{P_{xx}} \\
& \underbrace{-\frac{\partial}{\partial x}(\overline{\rho\, u''u''u''}) - \frac{\partial}{\partial z}(\overline{\rho\, u''u''w''})}_{TD_{xx}} \quad \underbrace{-2\frac{\partial}{\partial x}(\overline{u'p'})}_{PD_{xx}} \quad \underbrace{+2\frac{\partial}{\partial x}(\overline{u'\tau'_{xx}}) + 2\frac{\partial}{\partial z}(\overline{u'\tau'_{xz}})}_{VD_{xx}} \\
& \underbrace{-2\,\overline{u''}\left(\frac{\partial \overline{p}}{\partial x} - \frac{\partial \overline{\tau_{xx}}}{\partial x} - \frac{\partial \overline{\tau_{xz}}}{\partial z}\right)}_{M_{xx}} \underbrace{+2\left(\overline{p'\frac{\partial u'}{\partial x}}\right)}_{PS_{xx}} \underbrace{-2\,\overline{\tau'_{xx}\frac{\partial u'}{\partial x}} - 2\,\overline{\tau'_{xy}\frac{\partial u'}{\partial y}} - 2\,\overline{\tau'_{xz}\frac{\partial u'}{\partial z}}}_{DS_{xx}}.
\end{aligned} \tag{19}$$

$$\frac{\partial}{\partial t}(\overline{\rho v'' v''}) = \underbrace{-\frac{\partial}{\partial x}(\tilde{u}\,\overline{\rho v'' v''}) - \frac{\partial}{\partial z}(\tilde{w}\,\overline{\rho v'' v''})}_{MT_{yy}}$$
$$\underbrace{-\frac{\partial}{\partial x}(\overline{\rho\, v'' v'' u''}) - \frac{\partial}{\partial z}(\overline{\rho\, v'' v'' w''})}_{TD_{yy}} \quad \underbrace{+2\frac{\partial}{\partial x}(\overline{v'\tau'_{xy}}) + 2\frac{\partial}{\partial z}(\overline{v'\tau'_{yz}})}_{VD_{yy}}$$
$$\underbrace{-2\,\overline{v''}\left(-\frac{\partial\overline{\tau_{xy}}}{\partial x} - \frac{\partial\overline{\tau_{yz}}}{\partial z}\right)}_{M_{yy}} \underbrace{+2\left(\overline{p'\frac{\partial v'}{\partial y}}\right)}_{PS_{yy}} \underbrace{-2\,\overline{\tau'_{xy}\frac{\partial v'}{\partial x}} - 2\,\overline{\tau'_{yy}\frac{\partial v'}{\partial y}} - 2\,\overline{\tau'_{yz}\frac{\partial v'}{\partial z}}}_{DS_{yy}}, \tag{20}$$

$$\frac{\partial}{\partial t}(\overline{\rho w'' w''}) = \underbrace{-\frac{\partial}{\partial x}(\tilde{u}\,\overline{\rho w'' w''}) - \frac{\partial}{\partial z}(\tilde{w}\,\overline{\rho w'' w''})}_{MT_{zz}} \quad \underbrace{-2\,\overline{\rho u'' w''}\,\frac{\partial\tilde{w}}{\partial x} - 2\,\overline{\rho w'' w''}\,\frac{\partial\tilde{w}}{\partial z}}_{P_{zz}}$$
$$\underbrace{-\frac{\partial}{\partial x}(\overline{\rho\, w'' w'' u''}) - \frac{\partial}{\partial z}(\overline{\rho\, w'' w'' w''})}_{TD_{zz}} \quad \underbrace{-2\frac{\partial}{\partial z}(\overline{w'p'})}_{PD_{zz}} \quad \underbrace{+2\frac{\partial}{\partial x}(\overline{w'\tau'_{xz}}) + 2\frac{\partial}{\partial z}(\overline{w'\tau'_{zz}})}_{VD_{zz}}$$
$$\underbrace{-2\,\overline{w''}\left(\frac{\partial\overline{p}}{\partial z} - \frac{\partial\overline{\tau_{xz}}}{\partial x} - \frac{\partial\overline{\tau_{zz}}}{\partial z}\right)}_{M_{zz}} \underbrace{+2\left(\overline{p'\frac{\partial w'}{\partial z}}\right)}_{PS_{zz}} \underbrace{-2\,\overline{\tau'_{xz}\frac{\partial w'}{\partial x}} - 2\,\overline{\tau'_{yz}\frac{\partial w'}{\partial y}} - 2\,\overline{\tau'_{zz}\frac{\partial w'}{\partial z}}}_{DS_{zz}}, \tag{21}$$

$$\frac{\partial}{\partial t}(\overline{\rho u'' w''}) = \underbrace{-\frac{\partial}{\partial x}(\tilde{u}\,\overline{\rho u'' w''}) - \frac{\partial}{\partial z}(\tilde{w}\,\overline{\rho u'' w''})}_{MT_{xz}}$$
$$\underbrace{-\overline{\rho u'' u''}\,\frac{\partial\tilde{w}}{\partial x} - \overline{\rho u'' w''}\,\frac{\partial\tilde{w}}{\partial z} - \overline{\rho u'' w''}\,\frac{\partial\tilde{u}}{\partial x} - \overline{\rho w'' w''}\,\frac{\partial\tilde{u}}{\partial z}}_{P_{xz}}$$
$$\underbrace{-\frac{\partial}{\partial x}(\overline{\rho\, u'' u'' w''}) - \frac{\partial}{\partial z}(\overline{\rho\, u'' w'' w''})}_{TD_{xz}} \quad \underbrace{-\frac{\partial}{\partial z}(\overline{u'p'}) - \frac{\partial}{\partial x}(\overline{w'p'})}_{PD_{xz}}$$
$$\underbrace{+\frac{\partial}{\partial x}(\overline{u'\tau'_{xz}} + \overline{w'\tau'_{xx}}) + \frac{\partial}{\partial z}(\overline{u'\tau'_{zz}} + \overline{w'\tau'_{xz}})}_{VD_{xz}}$$
$$\underbrace{-\overline{u''}\left(\frac{\partial\overline{p}}{\partial z} - \frac{\partial\overline{\tau_{xz}}}{\partial x} - \frac{\partial\overline{\tau_{zz}}}{\partial z}\right) - \overline{w''}\left(\frac{\partial\overline{p}}{\partial x} - \frac{\partial\overline{\tau_{xx}}}{\partial x} - \frac{\partial\overline{\tau_{xz}}}{\partial z}\right)}_{M_{xz}} \underbrace{+\left(\overline{p'\frac{\partial u'}{\partial z}} + \overline{p'\frac{\partial w'}{\partial x}}\right)}_{PS_{xz}}$$
$$\underbrace{-\overline{\tau'_{xz}\frac{\partial u'}{\partial x}} - \overline{\tau'_{yz}\frac{\partial u'}{\partial y}} - \overline{\tau'_{zz}\frac{\partial u'}{\partial z}} - \overline{\tau'_{xx}\frac{\partial w'}{\partial x}} - \overline{\tau'_{xy}\frac{\partial w'}{\partial y}} - \overline{\tau'_{xz}\frac{\partial w'}{\partial z}}}_{DS_{xz}}. \tag{22}$$

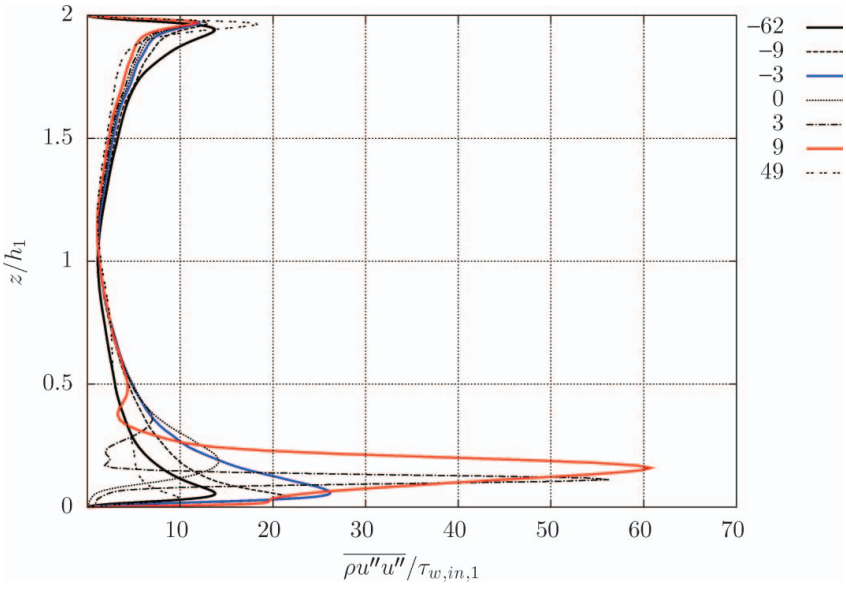

Figure 17. Profiles of normalized streamwise Reynolds stress at selected positions $(x - x_{sc})/h_2$. Symbols as in Figure 8.

The labels of various terms in Equations (19) to (22) have the following meaning: *MT*: mean transport, *P*: production, *TD*/*PD*: turbulent and pressure–diffusion, *VD*: viscous diffusion, *M*: mass flux contribution, *PS*: pressure–strain correlation and *DS*: turbulent dissipation.

The production term for the streamwise stress in Equation (19) consists of two terms, the first term describes production because of extra rate of mean strain, and the second one describes production because of mean shear. In front of the jet, where the flow decelerates, both terms are positive and act in the same direction, namely enhancing the streamwise stress. This can be seen in Figure 17 (blue curve), where the streamwise stress is plotted at selected positions $(x - x_{sc})/h_2$, normalized by the mean wall shear stress at inflow. Toward the upper wall, the flow accelerates and the first term of P_{xx} counteracts the second in such a way that their sum remains positive, but has a lower magnitude. This is part of the reason for the reduction of this stress. Downstream of the slot (Figure 17, red curve), the streamwise stress shows a main peak at $z/h_1 \approx 0.15$ (mixing layer below the jet, Figure 8) and two side-peaks, one close to the lower wall where the flow is reversed (Figure 9, $z/h_1 < 0.02$), and another at $z/h_1 \approx 0.5$. The streamwise stress at $z/h_1 \approx 0.15$ is by a factor of 4.5 larger than its peak value in the channel upstream. Even the reversed flow ($z/h_1 < 0.02$) exceeds this peak by a factor of 1.4. The reader might have noted that the production terms in Equations (19) to (22) contain gradients of Favre averaged mean velocities, while Figures 8, 9 and 11 show Reynolds-averaged mean velocities. At the present subsonic speeds there are, however, only negligible differences between the two so that our conclusions referring to mean velocity gradients are not affected.

There are two similar production terms P_{zz} in Equation (21) for the wall-normal stress, since the injected jet produces mean flow in z-direction. Both terms are, however, an order of magnitude smaller than the P_{xx}-terms so that these terms are not sufficient to discuss the behavior of the stress. $\overline{\rho w'' w''}$ also receives "energy" via redistribution from the streamwise

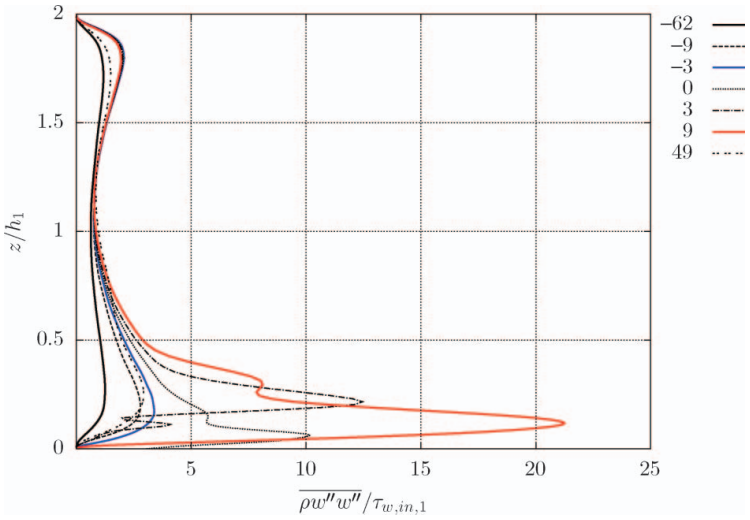

Figure 18. Profiles of normalized wall-normal Reynolds stress at selected positions $(x - x_{sc})/h_2$. Symbols as in Figure 8.

stress. Figure 18 shows profiles of the wall-normal stress, normalized the same way as the streamwise stress. From these profiles it can be concluded that $\overline{\rho w'' w''}$ is increased in front of the jet (blue curve) and peaks at $z/h_1 \approx 0.15$, where both production terms counteract and lead to a small negative sum (Figure 30). Taking into account that the dissipation term is negative as well (although its level is underestimated in an LES) and the remaining terms have divergence character, the velocity–pressure-gradient correlation, which is positive there (see Figure 31), must be responsible for the increase of the stress compared with its level upstream. At $(x - x_{sc})/h_2 = 9$, the shear layer below the jet and above produce the main peak at $z/h_1 \approx 0.12$ and a side-peak at $z/h_1 \approx 0.3$. In both zones P_{zz} and $(PD_{zz} + PS_{zz})$ are positive. The increase of the wall-normal stress near the upper wall can be explained with the growth of the second production term, $-2\,\overline{\rho w'' w''}\,\partial\tilde{w}/\partial z > 0$, because of the increase of the Reynolds stress itself and the positive gradient $\partial\tilde{w}/\partial x > 0$ of the first production term (Figure 37).

The Reynolds shear stress (see Equation (22) and Figure 19) undergoes production by mean shear and extra-rate-of-strain in two directions. It does not show great changes because of acceleration near the upper wall, but is enhanced upstream of the slot and changes sign twice downstream. Its negative peak at $(x - x_{sc})/h_2 = 9$, $z/h_1 \approx 0.15$ appears within the mixing layer below the jet with its steep positive velocity gradient, while the positive peak at $z/h_1 \approx 0.3$ lies within the mixing layer above the jet with its steep negative velocity gradient.

The spanwise Reynolds stress has no production term in its transport Equation (20) and receives its energy from the pressure–strain correlation only, since the pressure–diffusion term does not exist. Its behavior in front of the jet and downstream of the slot (blue and red curves in Figure 20) is very similar to that of the wall-normal stress. The position of the main peak below the mixing layer (red curve) lies in between the corresponding positions for the streamwise and wall-normal stresses. The value of the peak follows the usual hierarchy in temporal mixing layers, i.e., $\overline{\rho u'' u''}|_{\max} : \overline{\rho v'' v''}|_{\max} : \overline{\rho w'' w''}|_{\max} = 1 : 0.76 : 0.66$,

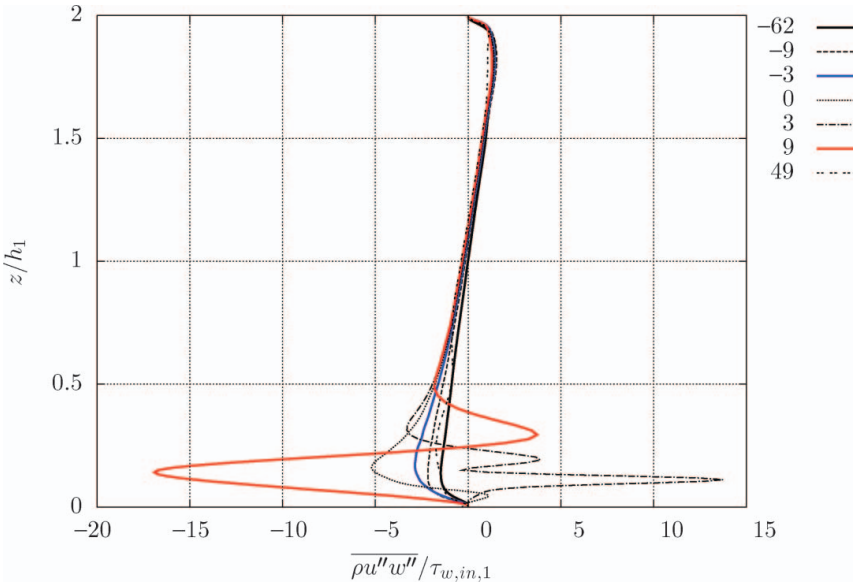

Figure 19. Profiles of normalized Reynolds shear stress at selected positions $(x - x_{sc})/h_2$. Symbols as in Figure 8.

only approximately, since the relation reads here $1 : 0.43 : 0.35$ and is a result of complex mechanisms that change the Reynolds stress anisotropy. The complexity of these mechanisms becomes visible when the second and third invariants, $II_b = -b_{ij}b_{ji}/2$ and $III_b = -b_{ij}b_{jk}b_{ki}/3$ of the Reynolds stress anisotropy tensor, $b_{ij} = \overline{\rho u_i'' u_j''}/\overline{\rho u_k'' u_k''} - \delta_{ij}/3$

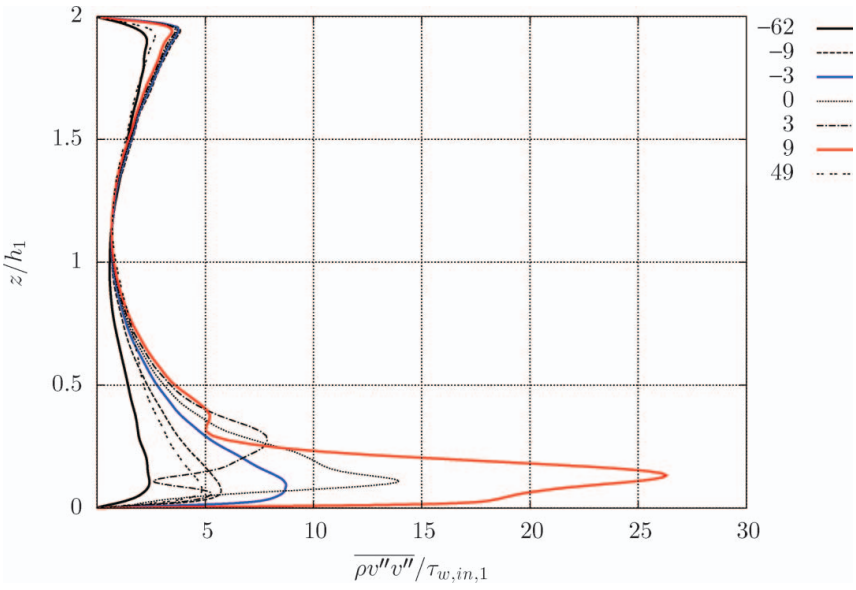

Figure 20. Profiles of normalized spanwise Reynolds stress at selected positions $(x - x_{sc})/h_2$. Symbols as in Figure 8.

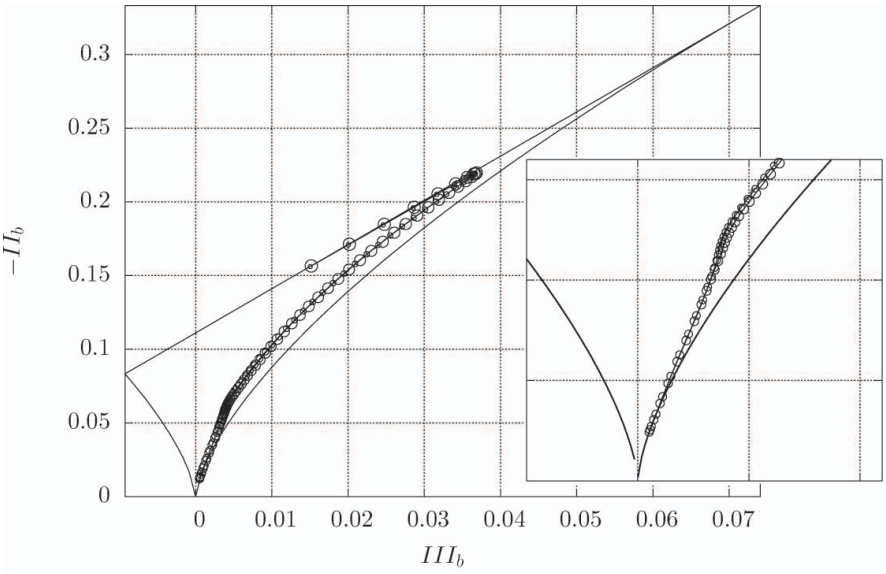

(a) Fully developed channel flow

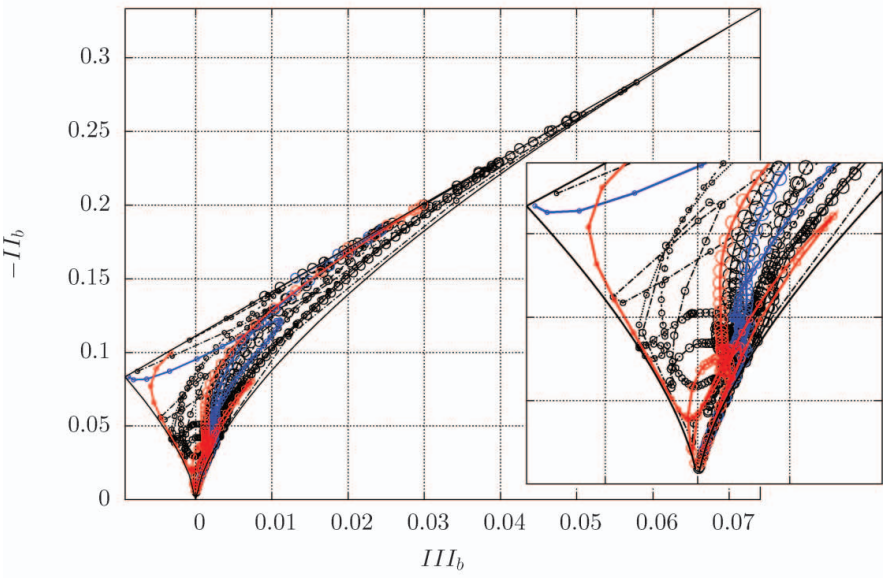

(b) Combustion channel (selected planes)

Figure 21. Invariants of the Reynolds stress anisotropy tensor (Lumley's map) for (a) fully developed channel flow, and (b) the planes $(x - x_{sc})/h_2 = -3$ (in blue) and $(x - x_{sc})/h_2 = 9$ (in red) of combustion channel. The symbols indicating the grid points increase in size from the lower to the upper channel wall.

are plotted in Lumley's map. Figure 21 shows this map for a fully developed channel flow (top) and the selected planes of the CC (bottom) for which the Reynolds stresses have been displayed. In case all grid points of the CC are plotted (not shown here), these points almost completely fill out the map; this can be already guessed from Figure 21(b).

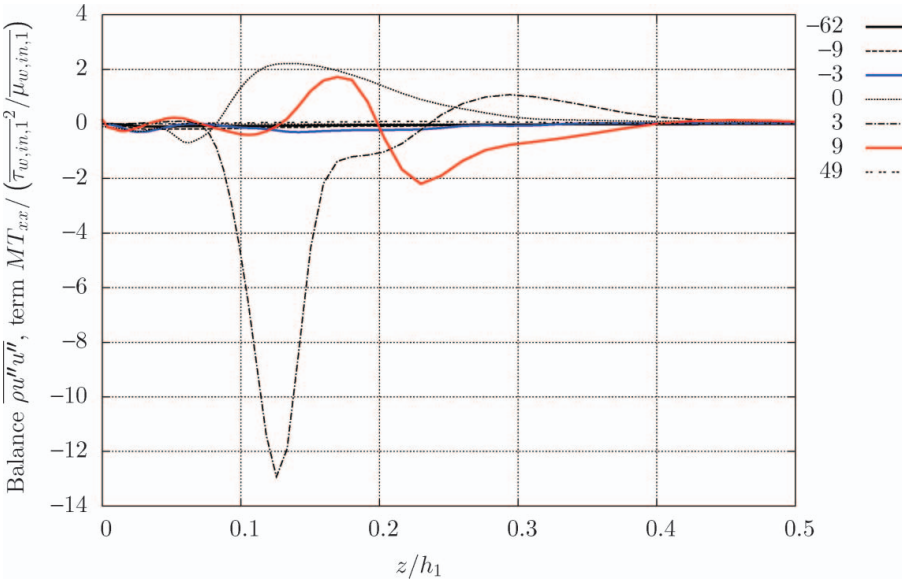

Figure 22. Profiles of mean transport MT_{xx} at selected positions $(x - x_{sc})/h_2$. Symbols as in Figure 8.

4.4. *Selected Reynolds stress transport terms*

Because of lack of space we focus on the discussion of selected transport terms only and split it into a discussion of effects in the vicinity of the injected jet and into acceleration effects near the upper wall. In both regions the streamwise Reynolds stress plays a key role in producing turbulent kinetic energy and redistributing it among the spanwise and wall-normal stresses. It therefore seems appropriate to present profiles of all its balance terms and to add profiles of a few source terms of the remaining three stresses. All terms shown below are normalized with $\bar{\tau}^2_{w,in,1}/\bar{\mu}_{w,in,1}$, the square of the wall shear stress at inflow and the constant viscosity at the wall there.

4.4.1. *Effects in the vicinity of the injected jet*

While the mean transport term, MT_{xx}, vanishes in fully developed channel flow, it changes sign several times in the vicinity of the injected jet. Its peak magnitude is of order 10, immediately downstream of the slot ($(x - x_{sc})/h_2 = 3$) and then it drops rapidly to peak values $\mathcal{O}(1)$ at $(x - x_{sc})/h_2 = 9$ (Figure 22).

The production term P_{xx} in Figure 23 has shapes at the blue and red positions, which strongly resemble those of $\overline{\rho u''u''}$ at both positions, except that the locations of the peaks differ slightly. While the maximum stress at $(x - x_{sc})/h_2 = 9$ exceeds its peak value far upstream by a factor of 4.5, the maximum production term is 40 times larger than its upstream value. Because of the action of other important terms, especially the velocity–pressure-gradient correlation, there is no one-to-one correspondence.

From DNS of fully developed compressible channel and pipe flow [32], we know that the turbulent diffusion term changes its sign twice between wall and centerline. This is also observed in the present LES (see Figure 24, black solid line). On the windward side of the jet (blue curve), we do not observe principal changes of this behavior, however an

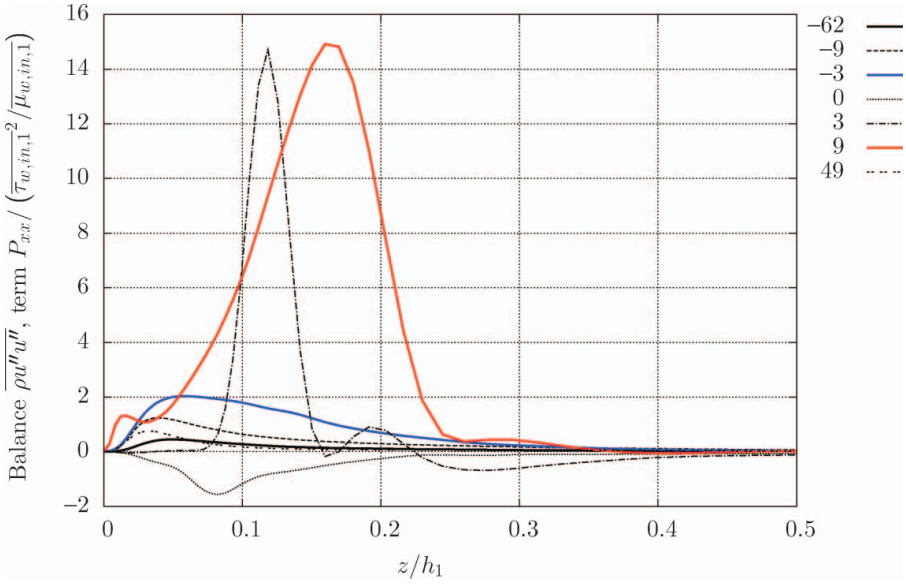

Figure 23. Profiles of production term P_{xx} at selected positions $(x - x_{sc})/h_2$. Symbols as in Figure 8.

increase in the magnitude of this term. Downstream of the slot (red curve), the number of sign changes of the term increases from 2 to 7 in the domain shown.

Pressure–diffusion, PD_{xx}, is zero far upstream, but has a strong negative peak where P_{xx} is strongly positive (Figure 25, red curve). So it counteracts production, like turbulent diffusion and dissipation (see below). On the jets windward side (blue curve), the behavior

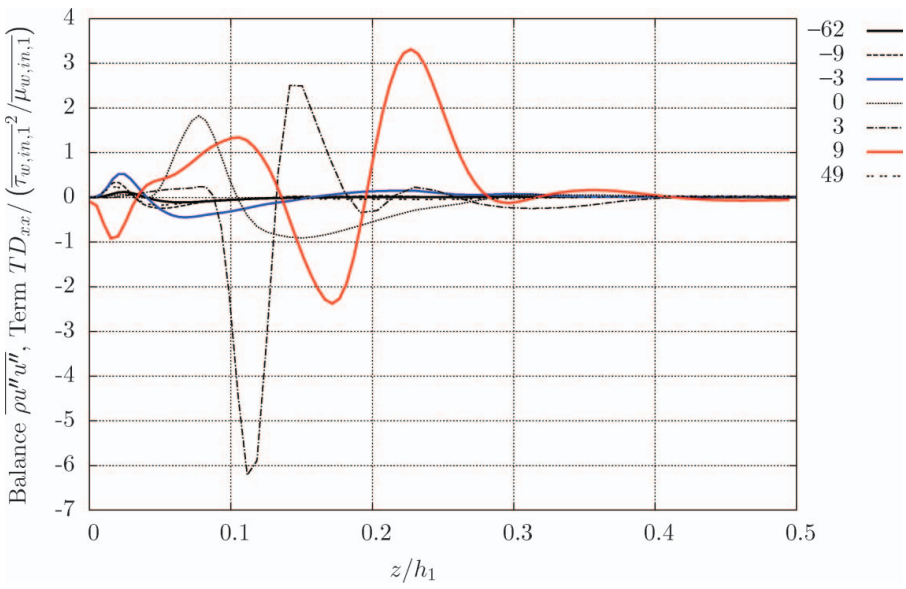

Figure 24. Profiles of turbulent diffusion term TD_{xx} at selected positions $(x - x_{sc})/h_2$. Symbols as in Figure 8.

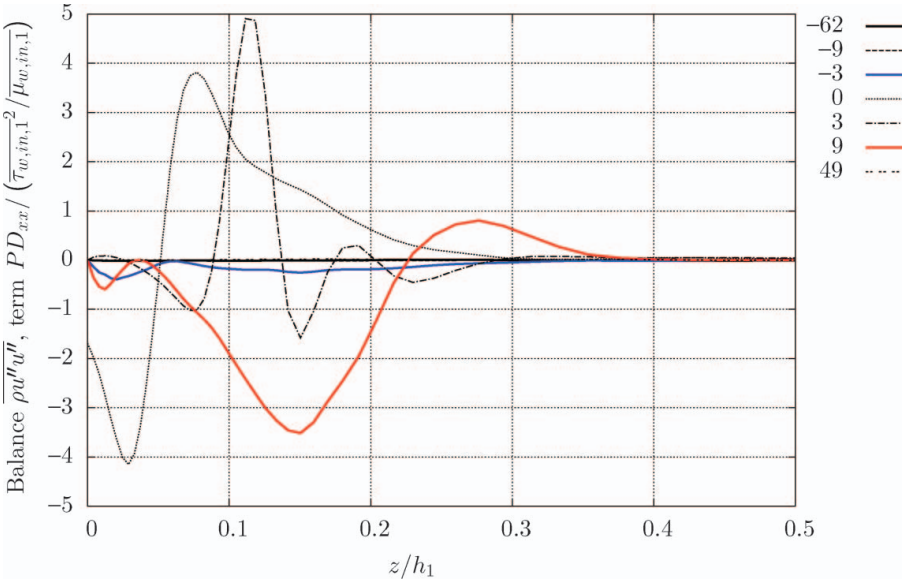

Figure 25. Profiles of pressure–diffusion term PD_{xx} at selected positions $(x - x_{sc})/h_2$. Symbols as in Figure 8.

is similar, except that there is no positive peak like on the red curve, which results from the upper mixing layer.

Viscous diffusion, VD_{xx}, is most important close to the wall (Figure 26), where it has a positive peak, which balances the negative peak of the turbulent dissipation rate (Figure 29). This is true for all profiles having wall boundary conditions. At $z/h_1 \approx 0.15$

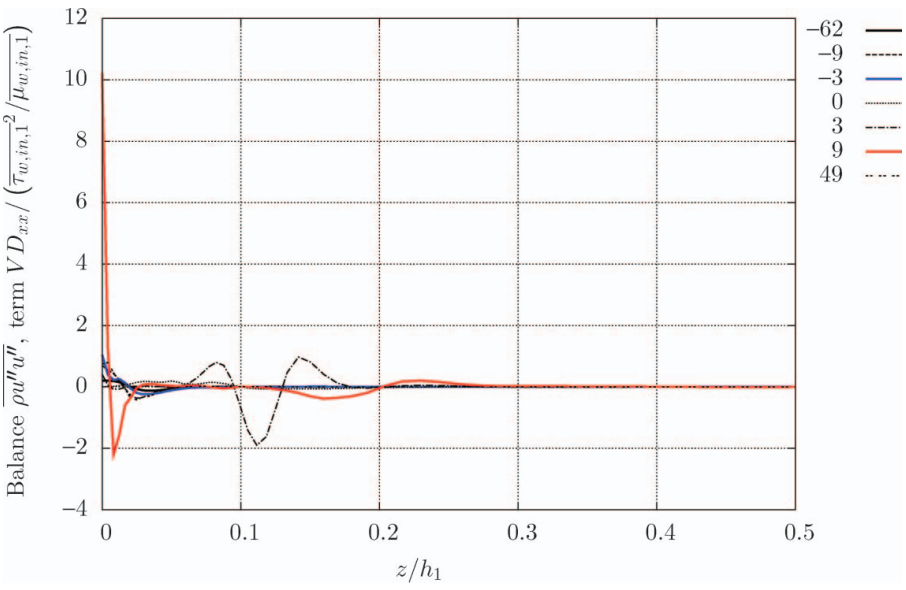

Figure 26. Profiles of viscous diffusion VD_{xx} at selected positions $(x - x_{sc})/h_2$. Symbols as in Figure 8.

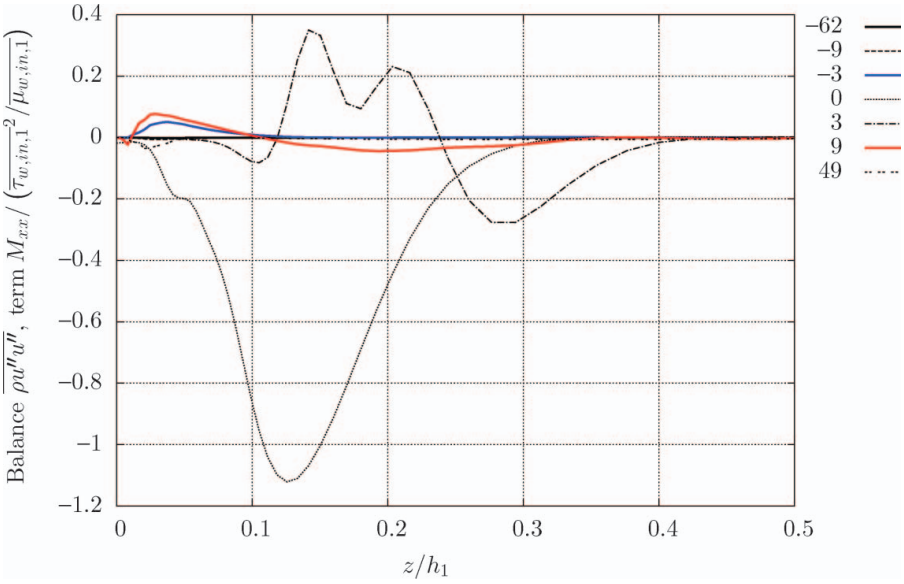

Figure 27. Profiles of mass-flux contribution M_{xx} at selected positions $(x - x_{sc})/h_2$. Symbols as in Figure 8.

(red curve), where production has its positive peak, TD_{xx}, PD_{xx}, PS_{xx}, VD_{xx} and DS_{xx} are all negative.

The mass-flux contribution M_{xx} in Figure 27 is unimportant not only far upstream but also on the windward side of the jet and downstream of the slot (blue and red curves). It is, however, of order 1 in the symmetry plane of the IC, and it is unclear whether this is due to the mass flux, $\overline{u''}$, itself or due to the gradients of mean pressure and/or viscous stress.

In the flow far upstream, PS_{xx} is zero at the wall and remains weakly negative between wall and symmetry plane. Its role is to transfer energy from the streamwise velocity fluctuations to the spanwise and wall-normal fluctuations. As a consequence, terms PS_{yy} and PS_{zz} are positive there. However, all three terms are so small that their variation is not visible on the present scale. In the vicinity of the injected jet, we observe a positive value of PS_{xx} where the flow is reversed (Figure 28, blue and red curves) and enhanced negative values because of flow deceleration (blue curve). The mixing layer on top of the downstream separation bubble generates an immense increase in magnitude of PS_{xx} at $z/h_1 \approx 0.17$ (red curve). It is of interest to combine the pressure–diffusion and pressure–strain terms to get the velocity–pressure-gradient correlation. This term (not shown) has two sign changes at $(x - x_{sc})/h_2 = 9$ and an even stronger negative peak.

We mention here again that an LES is generally not in a position to predict turbulent dissipation rates exactly because of the lack of unresolved scales. However, the results for DS_{xx} in Figure 29 are still useful, since they show the right trends when the flow is decelerated and undergoes high turbulence production in mixing layers. Hence, DS_{xx} is increased due to flow deceleration in front of the jet, in the wall layers of the reversed flow and in the mixing layer below the jet (red curve).

In the remaining part of this subsection we present profiles of production and velocity–pressure-gradient terms for the remaining Reynolds stresses in order to highlight their

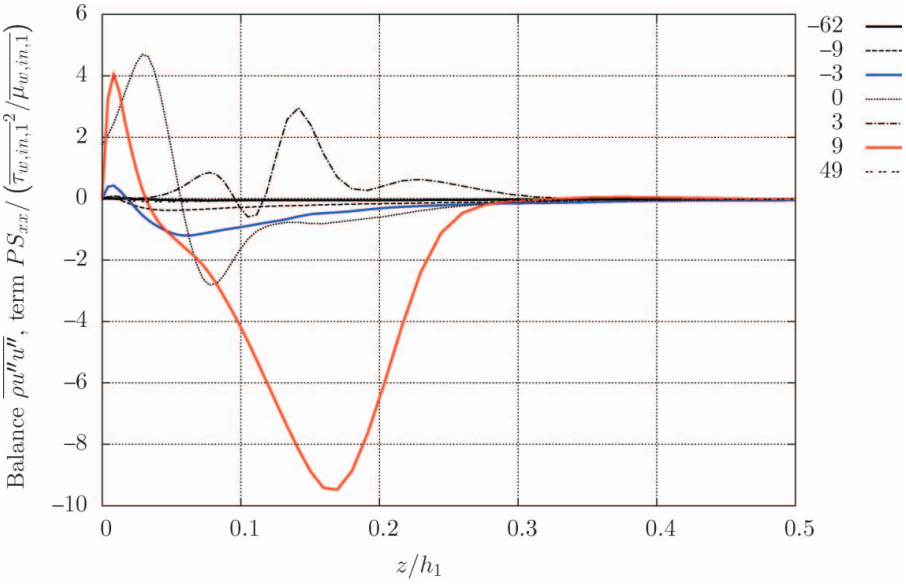

Figure 28. Profiles of pressure–strain correlation PS_{xx} at selected positions $(x - x_{sc})/h_2$. Symbols as in Figure 8.

behavior in the vicinity of the injected jet. Thereby we follow the order in which the stresses are presented above, $\overline{\rho u'' u''}$, $\overline{\rho w'' w''}$, $\overline{\rho u'' w''}$ and $\overline{\rho v'' v''}$.

Production of the wall-normal Reynolds stress in Figure 30 is an order of magnitude smaller than that of the streamwise component. On the windward side of the jet (blue curve)

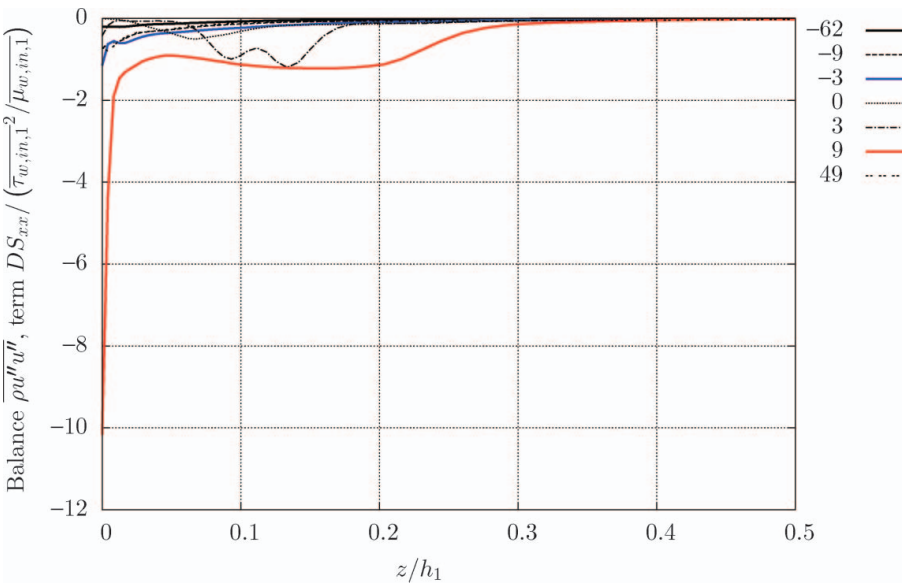

Figure 29. Profiles of dissipation rate DS_{xx} at selected positions $(x - x_{sc})/h_2$. Symbols as in Figure 8.

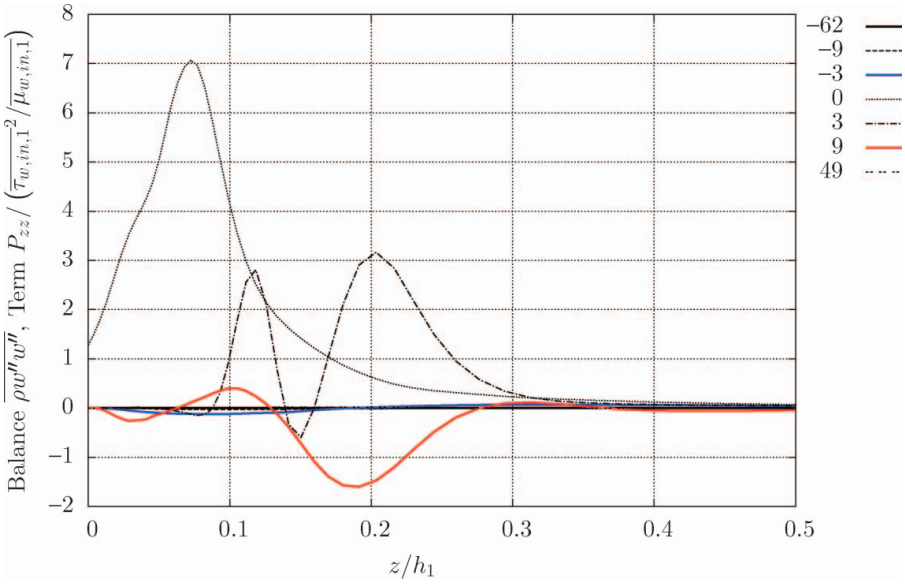

Figure 30. Profiles of production term P_{zz} at selected positions $(x - x_{sc})/h_2$. Symbols as in Figure 8.

it is negative for $z/h_1 < 0.19$, because the second production term $(-2\,\overline{\rho w'' w''}\,\partial\tilde{w}/\partial z)$ dominates the first production term $(-2\,\overline{\rho u'' w''}\,\partial\tilde{w}/\partial x)$. Above $z/h_1 = 0.19$, where the mean flow accelerates, P_{zz} is positive (see also the corresponding profile close to the upper wall). We present the sum of the pressure–diffusion and pressure–strain terms because they are usually modelled together. The reason is that their sum vanishes at the wall and may be small close to the wall, whereas the terms themselves show strong excursions. Figure 31 shows the velocity–pressure-gradient correlation.

Production of the Reynolds shear stress (Figure 32) has magnitudes comparable to those of the streamwise stress, but changes sign twice at $(x - x_{sc})/h_2 = 9$, following the sign changes of vertical gradients of $\tilde{u} \approx \bar{u}$ (see Figure 8). A similar sign change should appear at $(x - x_{sc})/h_2 = -3$ because of the tiny separation bubble there, but is not visible under the chosen scaling.

The velocity–pressure-gradient correlation $VPG_{xz} = (PD_{xz} + PS_{xz})$ is zero along the wall (Figure 33) and counteracts production away from the wall with slightly lower amplitudes, in agreement with DNS data of Le and Moin [33]. The dissipation rate of the Reynolds shear stress remains small compared to P_{xz} (not shown).

The spanwise Reynolds stress which is not produced ($P_{yy} = 0$) gets its "energy" from the streamwise stress via redistribution only (Figure 34). This is confirmed by the negative and positive peaks of the pressure–strain correlations PS_{xx} and PS_{yy} at $z/h_1 \approx 0.07$ (blue curve) and $z/h_1 \approx 0.15$ (red curve).

In the recirculation regions close to the wall where the flow points in the negative x-direction, PS_{zz} is negative, while PS_{xx} and PS_{yy} are positive. Hence, the streamwise and spanwise stress components receive energy from the wall-normal component. This mechanism has to do with the small imbalance between splat and anti-splat events, and is explained and modelled by Perot and Moin [34, 35].

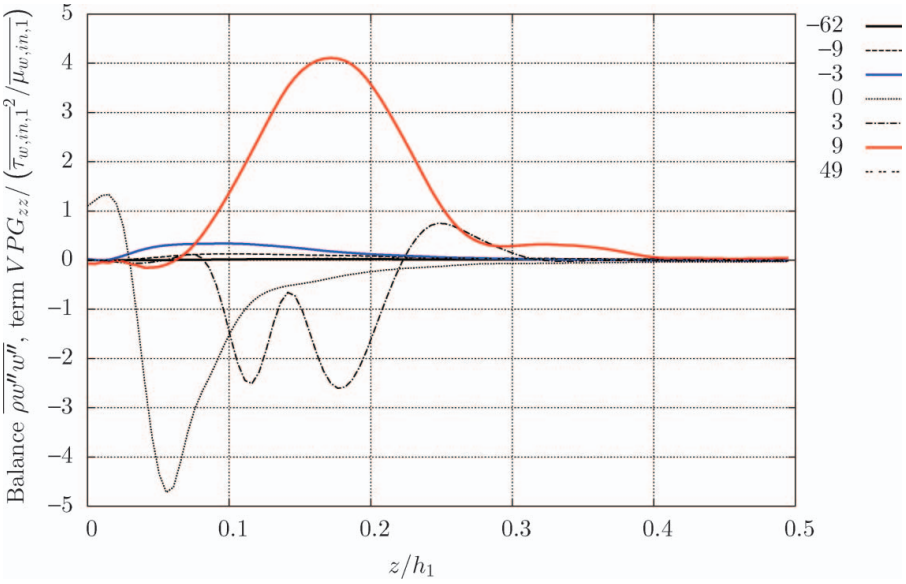

Figure 31. Profiles of the velocity–pressure-gradient correlation $VPG_{zz} = (PD_{zz} + PS_{zz})$ at selected positions $(x - x_{sc})/h_2$. An error of $\mathcal{O}(0.3)$ is observed in wall proximity. Symbols as in Figure 8.

The dissipation profiles DS_{yy} (not shown) reflect very similar features as those of fully developed channel flow, namely peak values at the wall, then minima, followed by relative maxima away from the wall, before the decay toward relatively low values in the channel core follows. A relative maximum away from the wall reflects vigorous turbulence activity in the mixing layer.

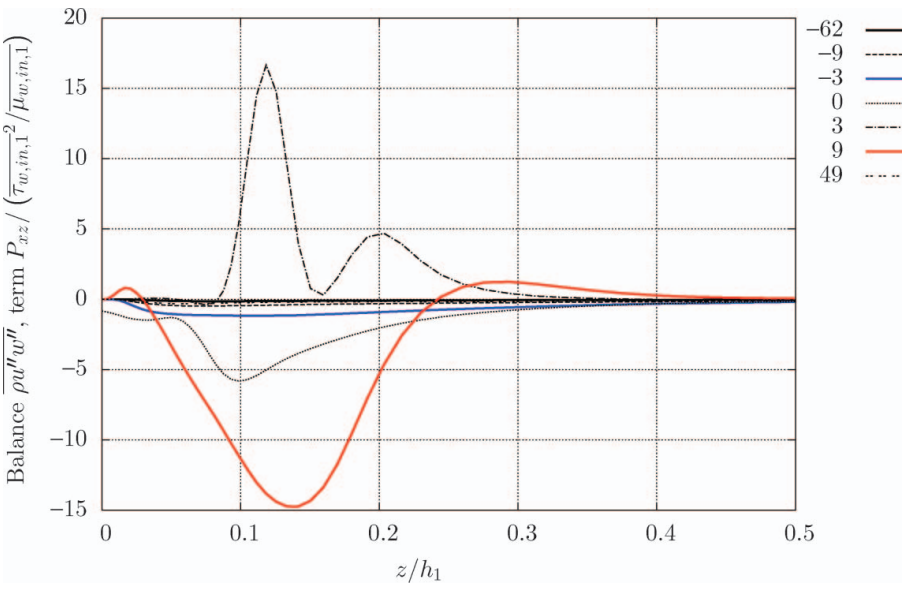

Figure 32. Profiles of production term P_{xz} at selected positions $(x - x_{sc})/h_2$. Symbols as in Figure 8.

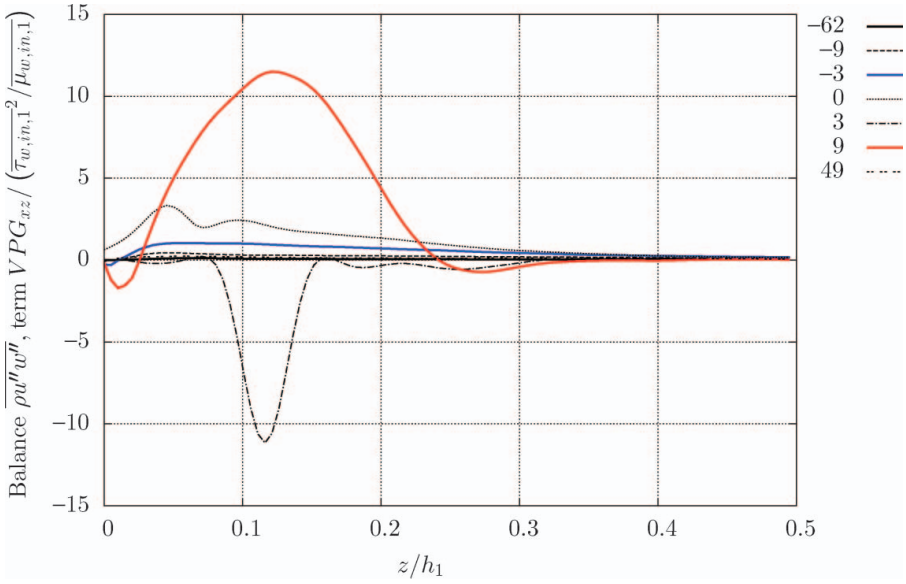

Figure 33. Profiles of the velocity–pressure-gradient correlation $VPG_{xz} = (PD_{xz} + PS_{xz})$ at selected positions $(x - x_{sc})/h_2$. Symbols as in Figure 8.

4.4.2. *Acceleration effects near the upper wall*

While discussing the behavior of Reynolds stresses we have already noted that the streamwise stress is decreased close to the upper wall because of flow acceleration, whereas the other normal stresses are increased compared to the incoming flow. The Reynolds shear

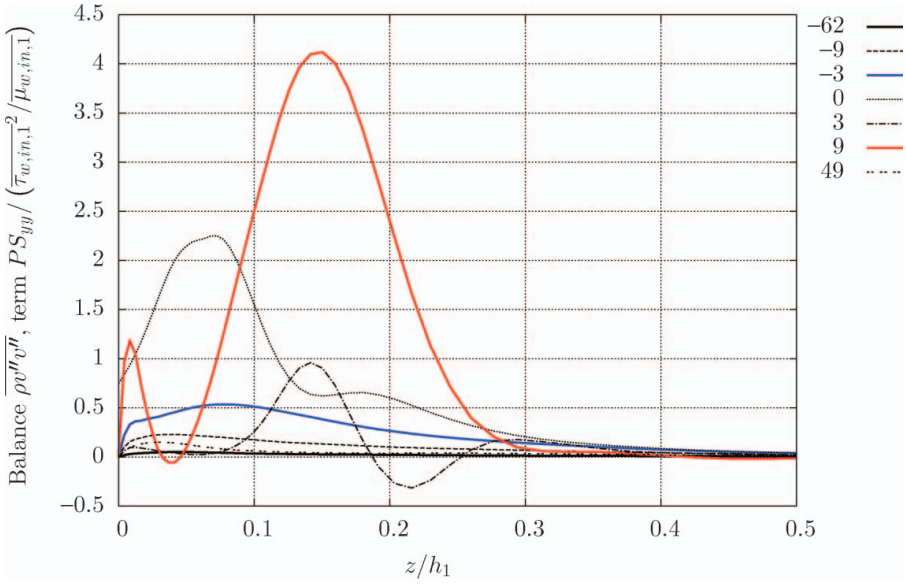

Figure 34. Profiles of pressure–strain correlation PS_{yy} at selected positions $(x - x_{sc})/h_2$. Symbols as in Figure 8.

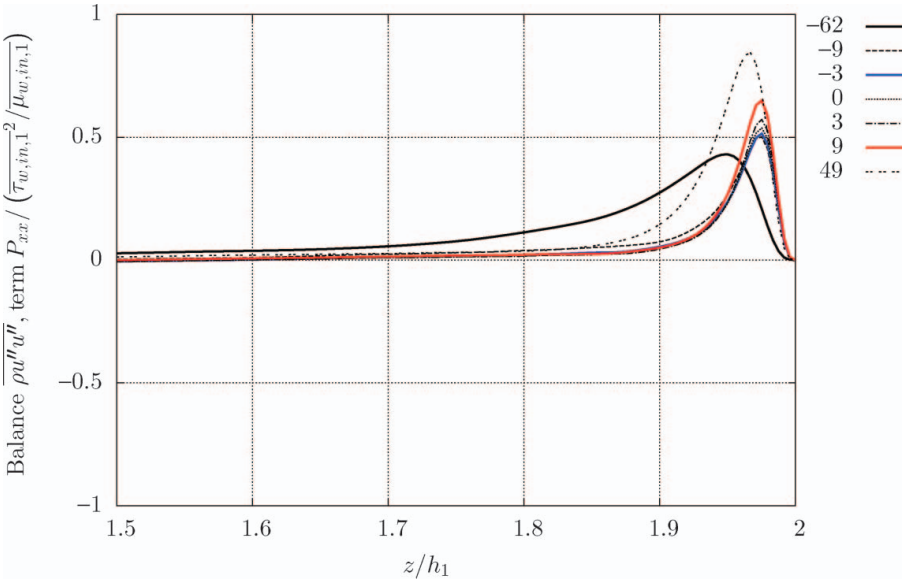

Figure 35. Profiles of production P_{xx} near the upper wall at selected positions $(x - x_{sc})/h_2$. Symbols as in Figure 8.

stress turns out to be only weakly affected. We will now see whether this behavior is supported by corresponding changes of the source/sink terms in the balance equations, namely production and velocity–pressure-gradient correlation.

Figure 35 confirms that the production of the streamwise Reynolds stress is reduced compared to fully developed channel flow over most of the upper channel quarter. Only close to the wall production because of mean shear dominates over negative production because of accelerating strain. This near-wall increase in production also causes an increase in near-wall velocity–pressure-gradient correlation (Figure 36) and dissipation (not shown). Further away from the upper wall, both terms are reduced, compared to their values far upstream.

Both production terms in the transport Equation (21) for $\overline{\rho w'' w''}$ provide positive contributions (see Figure 37). This mainly explains the increase of this stress compared to fully developed flow.

Production of the Reynolds shear stress in Figure 38 is increased in the whole domain shown, but especially close to the wall. There, terms 1 and 3 of the production term in Equation (22) are negative and hence counteract terms 2 and 4. Term 4 is larger than far upstream because the magnitude of $\partial \tilde{u}/\partial z$ and $\overline{\rho w'' w''}$ itself are increased.

The spanwise Reynolds stress has no production and no pressure–diffusion terms. The pressure–strain correlation in Figure 39 shows increased amplitudes, which are consistent with the increased amplitude of $(PD_{xx} + PS_{xx})$ there. An increased source for turbulence activity naturally also leads to increased dissipation rate, DS_{yy} (not shown).

4.5. *Mean total enthalpy transport*

The transport equation of total enthalpy, ensemble averaged in y-direction and time, reads in its differential form as

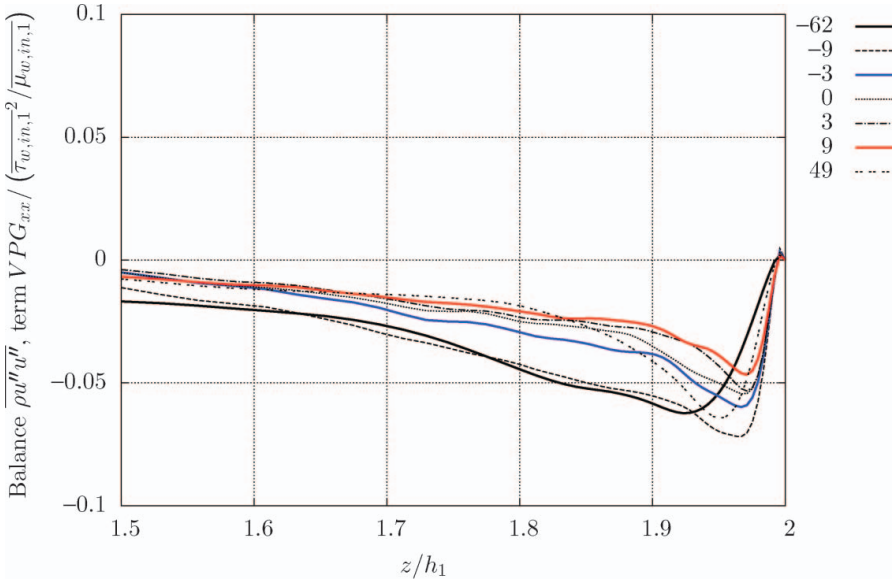

Figure 36. Profiles of the velocity–pressure-gradient correlation $VPG_{xx} = (PD_{xx} + PS_{xx})$ near the upper wall at selected positions $(x - x_{sc})/h_2$. Symbols as in Figure 8.

$$0 = \frac{\partial \overline{u_i \tau_{ix}}}{\partial x} + \frac{\partial \overline{u_i \tau_{iz}}}{\partial z} - \frac{\partial \overline{\rho u H}}{\partial x} - \frac{\partial \overline{\rho w H}}{\partial z} - \sum_{\alpha=1}^{N_s} \overline{\Delta h^0_{f,\alpha} \omega_\alpha}$$
$$- \frac{\partial \overline{q_x}}{\partial x} - \frac{\partial \overline{q_z}}{\partial z} + \frac{\partial}{\partial x} \sum_{\alpha=1}^{N_s} \overline{h_{s,\alpha} \frac{\mu}{Sc} \frac{dY_\alpha}{d\xi} \frac{\partial \xi}{\partial x}} + \frac{\partial}{\partial z} \sum_{\alpha=1}^{N_s} \overline{h_{s,\alpha} \frac{\mu}{Sc} \frac{dY_\alpha}{d\xi} \frac{\partial \xi}{\partial z}}. \tag{23}$$

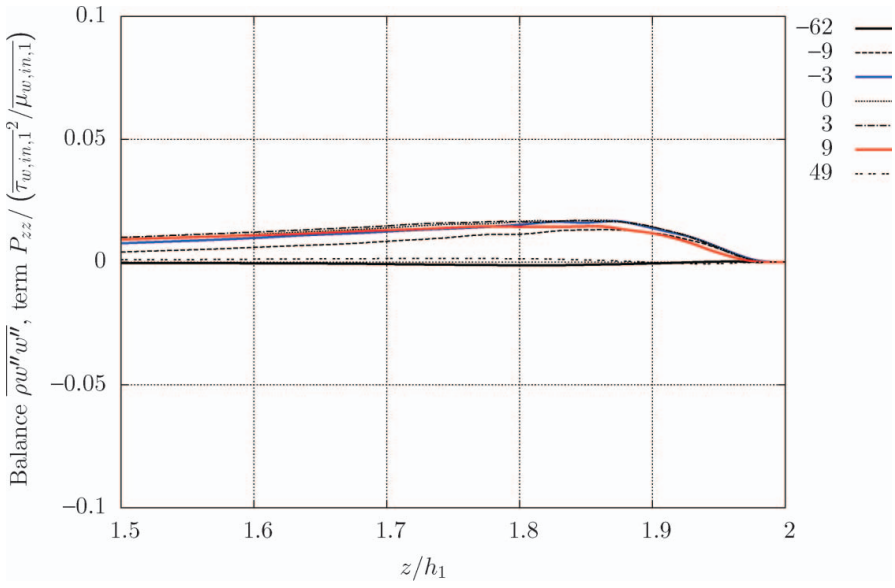

Figure 37. Profiles of the production term P_{zz} near the upper wall at selected positions $(x - x_{sc})/h_2$. Symbols as in Figure 8.

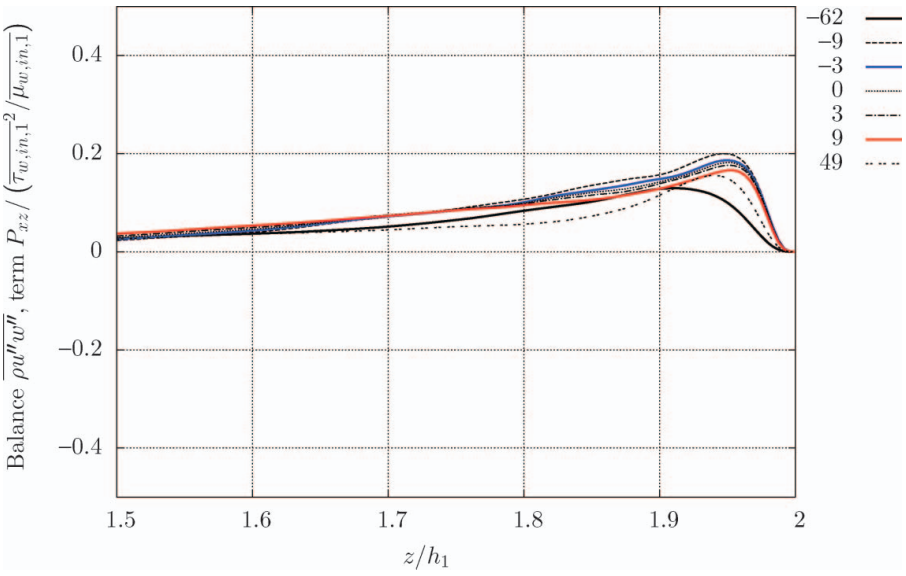

Figure 38. Profiles of the production term P_{xz} near the upper wall at selected positions $(x - x_{sc})/h_2$. Symbols as in Figure 8.

Integrating along the wall-normal direction, from a variable position z to the upper wall at $z = 2\,h_1$, and using the appropriate boundary conditions, in particular $\bar{q}_z(2\,h_1) = -\bar{q}_{w,o}$, yields

$$\begin{aligned}\bar{q}_{w,o} &= \underbrace{-\int_z^{2h_1} \frac{\partial\, \overline{u_i \tau_{ix}}}{\partial x}\, d\hat{z}}_{\varsigma_{1,x}} \underbrace{+\, \overline{u_i \tau_{iz}}}_{\varsigma_{1,z}} + \underbrace{\int_z^{2h_1} \frac{\partial\, \overline{\rho u H}}{\partial x}\, d\hat{z}}_{\varsigma_{2,x}} \underbrace{-\, \overline{\rho w H}}_{\varsigma_{2,z}} + \underbrace{\int_z^{2h_1} \sum_{\alpha}^{N_s} \overline{\Delta h^0_{f,\alpha} \omega_\alpha}\, d\hat{z}}_{\varsigma_3} \\ &\quad \underbrace{+\int_z^{2h_1} \frac{\partial \overline{q_x}}{\partial x}\, d\hat{z}}_{\varsigma_{4,x}} \underbrace{-\, \overline{q_z}}_{\varsigma_{4,z}} \underbrace{-\int_z^{2h_1} \frac{\partial}{\partial x} \sum_{\alpha=1}^{N_s} \overline{h_{s,\alpha} \frac{\mu}{Sc} \frac{dY_\alpha}{d\xi} \frac{\partial \xi}{\partial x}}\, d\hat{z}}_{\varsigma_{5,x}} \underbrace{+ \sum_{\alpha=1}^{N_s} \overline{h_{s,\alpha} \frac{\mu}{Sc} \frac{dY_\alpha}{d\xi} \frac{\partial \xi}{\partial z}}}_{\varsigma_{5,z}}.\end{aligned} \tag{24}$$

The labels in Equation (24) have the following meaning: $(\varsigma_{1,x}, \varsigma_{1,z})$: mean work done by viscous stresses in x- and z-directions, $(\varsigma_{2,x}, \varsigma_{2,z})$: mean convective flux of total enthalpy in x- and z-directions, ς_3: mean heat release term, $(\varsigma_{4,x}, \varsigma_{4,z})$: mean heat flux by conduction in x- and z-directions, $(\varsigma_{5,x}, \varsigma_{5,z})$: mean flux of sensible enthalpy by diffusion in x- and z-directions.

Among the many terms contributing to the total enthalpy balance in Equation (24), we discuss only two, namely the mean conductive heat flux at the upper and lower walls, and

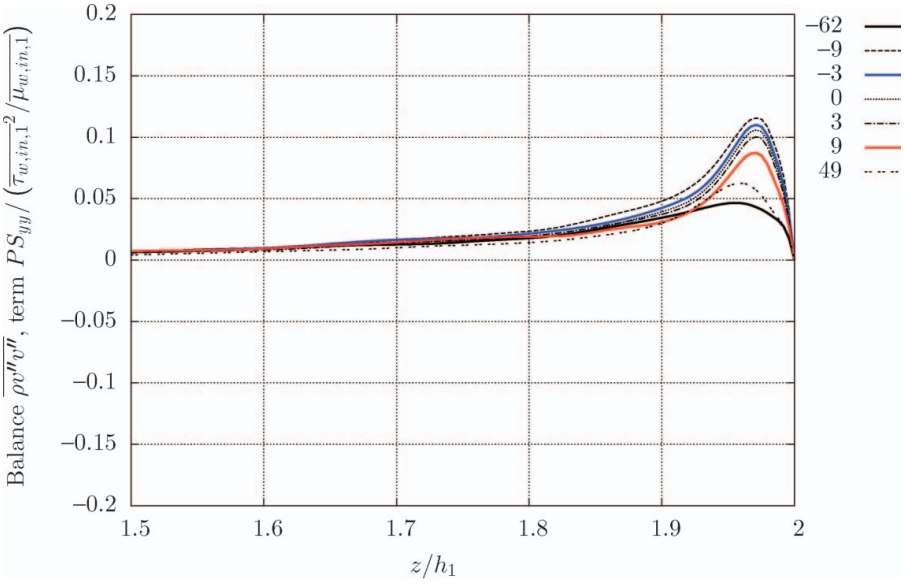

Figure 39. Profiles of pressure–strain correlation PS_{yy} near the upper wall at selected positions $(x - x_{sc})/h_2$. Symbols as in Figure 8.

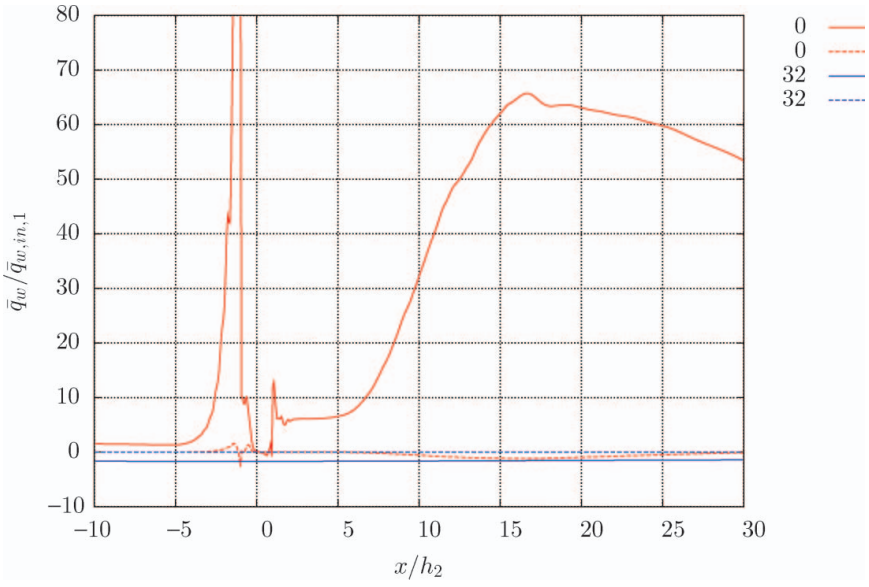

Figure 40. Streamwise development of mean wall-normal heat flux by conduction at the upper wall (blue curves, $z/h_2 = 32$) and lower wall (red curves, $z/h_2 = 0$). Continuous lines show $-\overline{\lambda \partial T/\partial z}$, while dashed lines represent $-\overline{\lambda' \partial T'/\partial z}$.

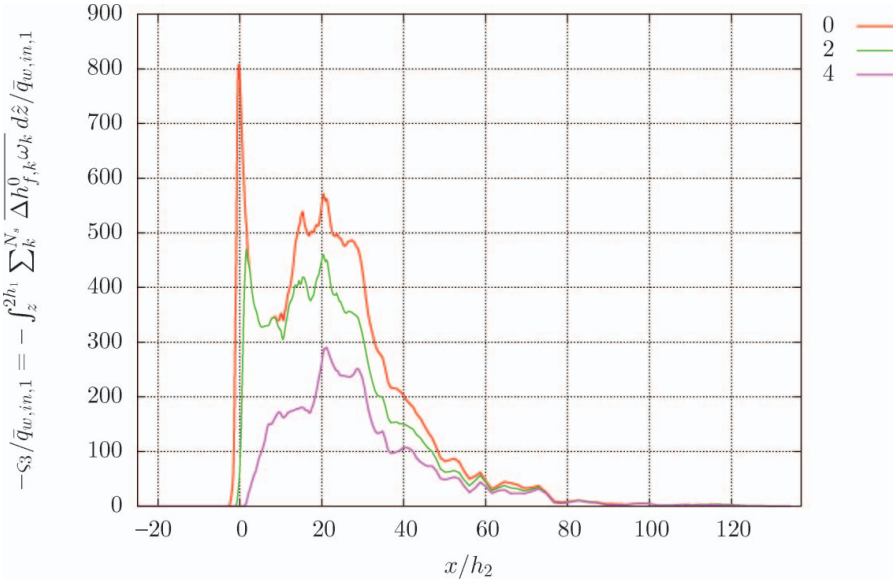

Figure 41. Streamwise development of integrated mean heat release term at different distances, $z/h_2 = 0, 2, 4$, from the lower main channel wall.

the integrated mean heat release term. The former is of practical importance, since it gives an impression where, along the wall, local high heat loads appear.

Figure 40 contains the mean wall-normal heat flux by conduction, normalized with the same flux far upstream where exists a non-reacting, fully developed channel flow. The plot not only shows the mean of the product of temperature gradient and thermal conductivity but also the correlation of their fluctuations, which turns out to be negligibly small. The red continuous curve reveals a strong peak of the mean molecular heat flux at the wall, just in front of the slot ($\bar{q}_w \approx 120\,\bar{q}_{w,in,1}$). This is also the position where the temperature has a peak in the tiny recirculation bubble (Figure 15, blue curve, $z/h_1 \approx 0.025$). Downstream of the slot, where the mean flow reattaches ($(x - x_{sc})/h_2 \approx 16.5$), another maximum is observed. It is due to the transport of hot burnt gas toward the wall. The relaxation of the wall heat flux toward a constant value needs a long distance, which cannot be provided in the computation. At $(x - x_{sc})/h_2 \approx 134$ (downstream end of domain), it is not yet completed and the mean wall heat flux has a value of roughly $\bar{q}_w \approx 13\,\bar{q}_{w,in,1}$.

Figure 41 shows the streamwise development of the integrated heat release term at different distances from the lower wall. It is clear from Figure 41 that the peak in the mean wall heat flux in front of the slot (Figure 40) is a result of heat release. We also recall that the concentration of water vapor, the end product of the chemical reaction assumed here, was high in front of the jet (see Figure 5). Downstream of the slot and beyond the reattachment of the mean flow, another peak in the integrated heat release term is observed, before rapid decay occurs, which brings the heat release mechanism to its end still within the computational box.

5. Summary

It is shown that the complex thermo-fluid-dynamical problem of a plane chemically reacting hydrogen jet, which is injected perpendicularly into a fully developed turbulent subsonic

air flow, can be predicted using LES and high-order compact numerical schemes for spatial discretization. Equilibrium chemistry is assumed to simplify the problem. The semi-implicit LES technique applied is based on approximate deconvolution and explicit modelling of the filtered heat release term. A precursor LES of fully developed turbulent channel flow with air as working gas generates realistic inflow conditions.

Results of instantaneous and statistically averaged flow variables, together with Reynolds stresses, their transport and the total enthalpy transport, are presented.

The condition that the bulk Mach number of the incoming flow is 0.5 and the outgoing flow should remain subsonic, limits the ratio of mean injected to upstream momentum flux to a low value of order $1/2$. Hence, the reacting plane jet does not penetrate deeply into the channel.

Snapshots of the local Mach number and temperature give an impression of flow acceleration and temperature increase because of heat release. Carpet plots and contour lines of local Mach number and water vapor concentration at two successive instants in time highlight the dynamics of mixing and reaction processes between jet and crossflow. Contours of the instantaneous flame front are shown in planes parallel to the wall, together with temperature and water vapor concentration. Interestingly, the temperature snapshots reveal pockets of unburnt jet fluid upstream of the sharp flame front.

Projections of instantaneous velocity vectors into the midplane of the side-channel, perpendicular to the crossflow, reflect the complexity of the turbulent mixing process between jet and crossflow and the rapid transition of the jet from a state of laminar flow to turbulence.

Mean values of velocity, density, pressure and temperature are presented in terms of contour plots and wall-normal profiles at selected positions in the neighborhood of the slot. They reveal a tiny recirculation zone upstream of the jet and a large one downstream of the slot. As a consequence of injection and reaction, air approaching the jet at a certain distance off the lower wall ($z/h_1 < 0.4$) is retarded, compressed and heated. Hence, its mean pressure rises over its value upstream. Very close to the wall, the heat release effect, however, dominates the compression effect and decreases the density. Toward the upper wall (at a streamwise distance corresponding to the midplane of the side channel), mean density, pressure and temperature are reduced, while the mean axial velocity is increased as a result of flow acceleration. Downstream of the slot, the flow field is controlled by recirculation effects, intense mixing dynamics and generation and transport of heat by reaction. The jet in crossflow therefore provides a variety of mechanisms to change Reynolds stresses, their generation and transport terms.

Accordingly, profiles of four Reynolds stresses, plotted at the same x-positions as the mean primitive variables, show dramatic increases in magnitude in the mixing layer above the rear recirculation zone. Effects of compression on the windward side of the jet have similar, although somewhat weaker amplification effects. Flow acceleration decreases the streamwise Reynolds stress, but enhances the other two normal stresses. Plotting the invariants of the Reynolds stress anisotropy tensor for all profiles selected into Lumley's map shows the complexity of this flow, compared with fully developed channel flow. The complexity in the Reynolds stress distribution, reflected in the drastic changes in its anisotropy, illustrates the difficulty faced in RANS modelling of this type of flow.

Explanations concerning the behavior of Reynolds stresses are provided by looking mainly at profiles of production, redistribution (or velocity–pressure-gradient) and dissipation terms, very well knowing that an LES cannot predict dissipation rates correctly, but is capable of describing trends because of various mechanisms with sufficient accuracy. A

work that remains to be done in the near future is to trace the behavior of redistribution terms back to the behavior of mean density as proposed by Foysi et al. [36].

Integration of the mean total enthalpy equation in wall-normal direction provides a means to study the integrated mean heat release term in planes parallel to the lower wall and to trace the peak in the wall heat flux immediately upstream of the slot back to heat of reaction. The chosen chemistry model indicates a strong heat release peak upstream of the injection slot. In reality, thermal fatigue could therefore play an important role there, making it necessary to choose materials properly or to try to optimize the geometrical features of the junction between CC and IC. Furthermore, repeating these simulations using more realistic chemistry would reveal extinction and re-ignition effects, and give further insight into the interplay of mixing and reaction.

Acknowledgements

The work has been supported by the German Research Association (DFG) within the framework of the research group GRK 1095/1 on "Aero-thermodynamic design of a scramjet propulsion system for future space transportation." Numerical simulations have been carried out using the high-performance computing system HLRB II (SGI Altix 4700) of Leibniz Rechenzentrum of the Bavarian Academy of Sciences at Garching, Germany.

References

[1] T.F. Fric and A. Roshko, *Vortical structure in the wake of a transverse jet*, J. Fluid Mech. 279 (1994), pp. 1–47.
[2] J. Andreopoulos and W. Rodi, *Experimental investigations of jets in a crossflow*, J. Fluid Mech. 138 (1984), pp. 93–127.
[3] D.T.H. New, T.T. Lim, and S.C. Luo, *On the effects of velocity profiles on the topological structure of a jet in cross flow*, in *First International Symposium on Turbulence and Shear Flow Phenomena, Santa Barbara, California, 1999*, S. Banerjee and J.K. Eaton, eds., Begell House, New York, 1999, pp. 647–652.
[4] J.W. Shan and P.E. Dimotakis, *Reynolds-number effects and anisotropy in transverse-jet mixing*, J. Fluid Mech. 566 (2006), pp. 47–96.
[5] L.K. Su and M.G. Mungal, *Simultaneous measurements of scalar and velocity field evolution in turbulent crossflowing jets*, J. Fluid Mech. 513 (2004), pp. 1–45.
[6] W.P. Jones and M. Wille, *Large-eddy simulation of a plane jet in a crossflow*, Int. J. Heat Fluid Flow 17 (1996), pp. 296–306.
[7] L.L. Yuan, R.L. Street, and J.H. Ferziger, *Large-eddy simulations of a round jet in crossflow*, J. Fluid Mech. 379 (1999), pp. 71–104.
[8] B. Wegner, Y. Huai, and A. Sadiki, *Comparative study of turbulent mixing in jet in cross-flow configurations using LES*, Int. J. Heat Fluid Flow 25 (2004), pp. 767–775.
[9] A. Sau, T.W.H. Sheu, R.R. Hwang, and W.C. Yang, *Three-dimensional simulation of square jets in cross-flow*, Phys. Rev. E 69 (2004), 066302.
[10] S. Muppidi and K. Mahesh, *Direct numerical simulation of round turbulent jets in crossflow*, J. Fluid Mech. 574 (2007), pp. 59–84.
[11] X. Guo, M. Meinke, and W. Schröder, *Large-eddy simulation of a jet in a crossflow*, in *Direct and Large-Eddy Simulation V*, R. Friedrich, B. Guerts and O. Metais, eds., Kluwer, München, Germany, 2004.
[12] P. Renze, M. Meinke, and W. Schröder, *Film cooling prediction by large eddy simulations*, Euromech Colloquium 469, Technische Universität Dresden, Germany, 2005.
[13] I.V. Iourokina and S.K. Lele, *Large eddy simulation of film cooling flow above a flat plate from inclined cylindrical holes*, Proceedings of FEDSM 2006, ASME Joint US-European Fluids Engineering Summer Meeting, Miami, FL, 2006.
[14] Y. Kamotani and I. Greber, *Experiments on confined turbulent jets in cross flow*, NASA Contractor Rep. CR-2392, NASA, Washington, DC, 1974.

[15] J.A. Denev, J. Fröhlich, and H. Bockhorn, *Direct numerical simulation of a transitional jet in crossflow with mixing and chemical reactions*, Proceedings of the Fifth International Symposium on Turbulence and Shear Flow Phenomena, München, Germany, 2007, pp. 1243–1248.

[16] J.A. Denev, J. Fröhlich, and H. Bockhorn, *Evaluation of mixing and chemical reactions within a jet in crossflow by means of LES*, Proceedings of the European Combustion Meeting, Louvain-la-Neuve, Belgium, 2005, pp. 1–6.

[17] J.B. McBride, S. Gordon, and M. Reno, *Coefficients for Calculating Thermodynamic and Transport Properties of Individual Species*, NASA Tech. Memo. 4513, NASA, Washington, DC, 1993.

[18] I. Mahle, *Direct and large-eddy simulation of inert and reacting compressible turbulent shear layers*, Ph.D. thesis, Technische Universität München, Germany, 2007.

[19] T. Poinsot and D. Veynante, *Theoretical and Numerical Combustion*, 2nd ed., Edwards, Camberley, UK, 2005.

[20] C. Pantano, S. Sarkar, and F.A. Williams, *Mixing of a conserved scalar in a turbulent reacting shear layer*, J. Fluid Mech. 481 (2003), pp. 291–328.

[21] N. Peters, *Laminar diffusion flamelet models in non-premixed turbulent combustion*, Prog. Energy Combust. Sci. 10 (1984), pp. 319–339.

[22] A. Ern and V. Giovangigli, *Fast and accurate multicomponent transport property evaluation*, J. Comput. Phys. 120 (1995), pp. 105–116.

[23] W.H. Press, S.A. Teukolsky, W.T. Vetterling, and B.P. Flannery, *Numerical Recipes in Fortran 77: The Art of Scientific Computing*, 2nd ed., Cambridge University Press, Cambridge, UK, 1992.

[24] J. Mathew, R. Lechner, H. Foysi, J. Sesterhenn, and R. Friedrich, *An explicit filtering method for LES of compressible flows*, Phys. Fluids 15 (2003), pp. 2279–2289.

[25] S.K. Lele, *Compact finite difference schemes with spectral-like resolution*, J. Comput. Phys. 103 (1992), pp. 16–42.

[26] C. Schaupp and R. Friedrich, *Large-eddy simulation of a plane reacting jet transversely injected into supersonic turbulent channel flow*, Int. J. Comput. Fluid. Dyn. 24 (2010), pp. 407–433.

[27] R.W. Bilger, *Turbulent flows with nonpremixed reactants*, in *Turbulent Reacting Flows*, P.A. Libby and F.A. Williams, eds., Springer-Verlag, Berlin, Germany, 1980, pp. 65–113.

[28] C.A. Kennedy, M. Carpenter, and R. Lewis, *Low–Storage, Explicit Runge–Kutta Schemes for the Compressible Navier–Stokes Equations*, ICASE Rep. 99-22, NASA Langley Research Center, Hampton, VA, 1999.

[29] J. Sesterhenn, *A characteristic-type formulation of the Navier–Stokes equations for high order upwind schemes*, Comput. Fluids 30 (2001), pp. 37–67.

[30] J.M. Floryan and L. Czechowski, *On the numerical treatment of corner singularity in the vorticity field*, J. Comput. Phys. 118 (1995), pp. 222–228.

[31] Z. Yosibash, M. Arad, A. Yakhot, and G. Ben-Dor, *An accurate semi-analytic finite difference scheme for two-dimensional elliptic problems with singularities*, Numer. Methods Partial Differ. Equ. 14 (1998), pp. 281–296.

[32] S. Ghosh, H. Foysi, and R. Friedrich, *Compressible turbulent channel and pipe flow: Similarities and differences*, J. Fluid Mech. 648 (2010), pp. 155–181.

[33] H. Le and P. Moin, *Direct numerical simulation of turbulent flow over a backward–facing step*, Tech. Rep. TF-58, Thermosciences Division, Department of Mechanical Engineering, Stanford University, California, 1994.

[34] B. Perot and P. Moin, *Shear-free turbulent boundary layers. Part 1: Physical insights into near-wall turbulence*, J. Fluid Mech. 295 (1995), pp. 119–227.

[35] B. Perot and P. Moin, *Shear-free turbulent boundary layers. Part 2: New concepts for Reynolds stress transport equation modelling in inhomogeneous flows*, J. Fluid Mech. 295 (1995), pp. 229–245.

[36] H. Foysi, S. Sarkar, and R. Friedrich, *Compressibility effects and turbulence scalings in supersonic channel flow*, J. Fluid Mech. 509 (2004), pp. 207–216.